

# Gravitational waves from scattering of stellar-mass black holes in galactic nuclei

Ryan M. O’Leary<sup>1\*</sup>, Bence Kocsis<sup>1,2†</sup>, and Abraham Loeb<sup>1‡</sup>

<sup>1</sup>*Harvard-Smithsonian Center for Astrophysics, 60 Garden St., Cambridge, MA 02138, USA*

<sup>2</sup>*Institute for Advanced Study, Einstein Drive, BH-151, Princeton, NJ 08540*

26 November 2024

## ABSTRACT

Stellar mass black holes (BHs) are expected to segregate and form a steep density cusp around supermassive black holes (SMBHs) in galactic nuclei. We follow the evolution of a multi-mass system of BHs and stars by numerically integrating the Fokker-Planck energy diffusion equations for a variety of BH mass distributions. We find that the BHs “self-segregate”, and that the rarest, most massive BHs dominate the scattering rate closest to the SMBH ( $\lesssim 10^{-1}$  pc). BH–BH binaries form out of gravitational wave emission during BH encounters. We find that the expected rate of BH coalescence events detectable by Advanced LIGO is  $\sim 1 - 10^2 \text{ yr}^{-1}$ , depending on the initial mass function of stars in galactic nuclei and the mass of the most massive BHs. We find that the actual merger rate is likely  $\sim 10$  times larger than this due to the intrinsic scatter of stellar densities in many different galaxies. The BH binaries that form this way in galactic nuclei have significant eccentricities as they enter the LIGO band (90% with  $e > 0.9$ ), and are therefore distinguishable from other binaries, which circularise before becoming detectable. We also show that eccentric mergers can be detected to larger distances and greater BH masses than circular mergers, up to  $\sim 700 M_{\odot}$ . Future ground-based gravitational wave observatories will be able to constrain both the mass function of BHs and stars in galactic nuclei.

**Key words:** galaxies:kinematics and dynamics–galaxies:nuclei–black hole physics–gravitational waves

## 1 INTRODUCTION

### 1.1 Motivation

The coalescence of stellar mass black hole–black hole (BH–BH) binaries is one of the most anticipated sources of gravitational waves for ground-based interferometers such as LIGO<sup>1</sup> or VIRGO<sup>2</sup>. Whether formed primordially (Belczynski et al. 2002, 2004; Sadowski et al. 2008) or in dense star clusters (Portegies Zwart & McMillan 2000; Gültekin et al. 2004; O’Leary et al. 2006; Gültekin et al. 2006; O’Leary et al. 2007; Miller & Lauburg 2008), nearly all of these binaries are expected to be circularised by gravitational wave (GW) emission before they are detectable by ground based observatories (O’Leary et al. 2006; Gültekin et al. 2006). In order to be detected with a high signal-to-noise ratio, matched filtering algorithms sift

through the LIGO data stream looking for such circular inspirals (Abbott et al. 2008), but might miss many eccentric events (Martel & Poisson 1999; Tessmer & Gopakumar 2007; Mandel et al. 2008). In principle, eccentric inspirals are well suited for detection as well, however they have not been expected to be a significant source for terrestrial detectors (except see Wen 2003).

In this paper, we propose an important additional source of gravitational wave sources, which preferentially form binaries that are still eccentric as they merge. In galactic nuclei with supermassive black holes (SMBH) of mass  $M_{\text{SMBH}} < 10^7 M_{\odot}$ , relaxation times are often less than a Hubble time, and can result in the formation of steep density cusp of stars and stellar mass black holes (BHs). Indeed, as many as  $\sim 20,000$  BHs are expected to have segregated into the inner  $\approx 1$  pc of the Milky Way (Morris 1993; Miralda-Escudé & Gould 2000; Freitag et al. 2006; Hopman & Alexander 2006b, hereafter HA06). When two BHs have a close encounter, they can release sufficient amount of energy in GWs to form a tight binary, and merge in less than a few hours. These mergers are almost always eccentric, in contrast to circular inspirals expected in globular

\* E-mail:roleary@cfa.harvard.edu

† E-mail:bkocsis@ias.edu

‡ E-mail:aloeb@cfa.harvard.edu

<sup>1</sup> <http://www.ligo.caltech.edu/>

<sup>2</sup> <http://www.virgo.infn.it/>

clusters. A similar process can occur in the runaway growth of BHs when no SMBH is present that will also result in eccentric mergers; however, such systems are inherently unstable and not long-lived (Quinlan & Shapiro 1987, 1989, 1990; Lee 1993).

The GWs generated during the evolution of these orbits are endowed with a rich structure. For sufficiently small impact parameters, the GWs can be detected with second generation GW instruments already during first passage (Kocsis et al. 2006). Subsequently, the eccentricity is close to unity for several thousand orbits after the formation of the binary, generating a train of short-duration distinct GW bursts with a continuous frequency spectrum. As the eccentricity gradually decreases, the separation between subsequent bursts decreases, and the waveform becomes continuous in the time-domain and decouples into discrete harmonics in frequency. Interestingly, as we show below, the eccentricity is non-negligible all the way to coalescence. The full waveform, consisting of a correlated set of distinct GW bursts, which evolves into a continuous eccentric inspiral signal, would not be discovered in the GW data by existing data analysis techniques such as GW burst search algorithms, nor by small eccentricity inspiral templates, since the contribution of individual bursts to the GW power is small and the contribution of higher harmonics is significant throughout the evolution (see Yunes et al. 2008, for a similar discussion for extreme mass ratio GW bursts during encounters with a supermassive black hole).

Eccentric inspirals are more luminous in GWs than circular inspirals and extend to higher frequencies, and so may be detectable to higher redshifts. Furthermore, these events may be capable of detecting intermediate mass black holes using terrestrial instruments (Brown et al. 2007; Mandel et al. 2008). The evolution of the signal during the initial phase of eccentric inspirals can be described using a small number of parameters, allowing one to construct very efficient and sensitive data analysis algorithms to search for these signals in the LIGO data. Additionally, these signals spend a longer physical time in the LIGO band, possibly reducing the false alarm rate for a fixed number of templates that cover the observational period. The modulation introduced by the Earth’s rotation during such an event can be utilised to further improve the measurement accuracy for the source position.

The GW waveforms have been studied for eccentric inspirals through several different approaches. Post-Newtonian (PN) waveforms exist up to 1.5PN order beyond the leading order gravitational radiation effects ( $\propto v^3$ ) for general mass ratios with spins (Vasuth & Majar 2007; Majar & Vasuth 2008), 2PN without spins (Damour et al. 2004, ( $\propto v^4$ , including the effects of eccentricity and radiation reaction) and 3PN including eccentricity but without spins and also neglecting radiation reaction ( $\propto v^6$ , Arun et al. 2008, and references therein), 5.5PN for extreme mass ratios without spins ( $\propto v^{11}$ , Tanaka et al. 1996). The evolution of a binary is chaotic at (or beyond) the 2PN approximation if the component BHs have spins (Levin 2006; Wu & Xie 2007) and also possibly for nonspinning BHs approaching the unstable circular orbit (Pretorius & Khurana 2007; Washik et al. 2008, i.e. exhibiting zoom-whirl orbits). Numerical relativity has mostly focused on the circular inspiral for comparable mass BHs (Baker et al. 2007;

Berti et al. 2007; Boyle et al. 2008, and references therein), or extreme mass ratios (Martel 2004; Pretorius & Khurana 2007; Babak et al. 2007). Recently, however, the waveforms have been evaluated for a handful of equal mass eccentric initial conditions (Sperhake et al. 2007; Washik et al. 2008; Hinder et al. 2008a,b).

In this paper, we perform two separate analyses to two different problems. First, in § 2, we determine the multi-mass distribution of BHs in galactic nuclei for a variety of mass models. In § 3, we determine the formation rate of binaries due to gravitational wave capture in a variety of galactic nuclei. In § 4 we describe the general features of the generated GW waveform, calculate the expected signal-to-noise ratio for its detection with second generation terrestrial GW instruments and determine the expected detection rate of such mergers. We also show that the eccentricity distribution of such sources will distinguish binaries formed in the manner outlined in this paper from BH-BH binaries formed dynamically in massive star clusters.

## 2 MASS SEGREGATION

Bahcall & Wolf (1976, hereafter BW76) were the first to correctly analyse the relaxation of a stellar population around a central point mass, although their analysis was highly idealised. They first derived the Fokker-Planck equations for a spherically symmetric distribution of a single-mass population of low mass stars around a massive black hole ( $M_* \ll M_{\text{SMBH}}$ ). They found that after about one half of a relaxation timescale the mass density profile of stars reaches a steady-state and forms a power-law cusp with respect to radius,  $\propto r^{-\alpha}$ , around the massive central object, with  $\alpha = 7/4$ . In a second paper, they extended their analysis to look at a multi-mass system and included effects of the loss-cone (Shapiro & Lightman 1976) that results from the disruption of stars by the central black hole (Bahcall & Wolf 1977, hereafter BW77). They found that in a two-mass system the more massive objects segregate from the lower mass stars by forming a steeper power-law density profile than the stars. This is in stark contrast to the evolution of a two-mass cluster of stars without a SMBH, which can eventually lead to the so-called Spitzer-instability (Spitzer 1969), in which the high mass stars decouple from the low mass objects entirely.

For a population of stars that are sufficiently old ( $\gtrsim 100$  Myr), stellar mass BHs with mass  $\sim 10 M_\odot$  are expected to become the most massive objects in the system and will begin to segregate from the main sequence stars due to dynamical friction (Morris 1993). Looking at our own Galactic Center and using a typical stellar mass function, Miralda-Escudé & Gould (2000) estimated that  $\sim 2.5 \times 10^4$  BHs should have segregated into the inner pc. Indeed, HA06 followed the work of BW77 by solving the time dependent Fokker-Planck equations and confirmed these results. They found that  $\sim 18,000$  BHs of  $10 M_\odot$  each, should segregate to form a steep density cusp around the SMBH in our galaxy, Sgr A\*, with  $\alpha_{\text{BH}} \approx 2$ , and that the stars and lighter compact objects form a shallower cusp with  $\alpha_* \approx 1.4$ .

Freitag et al. (2006, hereafter FAK06) have so far provided the most robust analysis of the segregation and distribution of a multi-mass system of BHs and stars in the

nuclei of galaxies (for a review, see Amaro-Seoane et al. 2007). The authors combined large  $N \sim 10^6$  Monte-Carlo Fokker-Planck simulations with a population synthesis code (Belczynski et al. 2002) to simulate the segregation and subsequent formation of a density cusp for an old population of stars. Their simulations were in remarkably good agreement with previous analyses (e.g. Morris 1993; Miralda-Escudé & Gould 2000, HA06). In their simulations of a Milky-Way-like galactic nucleus they found a similar overall number of stellar mass BHs ( $\sim 20,000$ ) within 1 pc of a  $3.5 \times 10^6 M_\odot$  SMBH. However, they found the BHs follow a slightly shallower density profile than HA06, with  $\alpha_{\text{BH}} \approx 1.8$ . Despite the level of detail in the simulations of FAK06, the simulations still have their limitations. Because of the large range in scales needed to follow the mass segregation, and subsequently the large number of particles in that volume, each star cannot be modelled by a single particle. The densest, most interesting regions of their simulations still suffer from small number statistics, and can't reveal the precise expectations for the mass distribution of stars and BHs. In order to calculate the rate of gravitational wave capture events one needs to apply a high-resolution method (like HA06) to multi-mass distribution of BHs for calculating the rates and detectability of the events.

Although the BHs are expected to dominate relaxation and dynamical encounters in the inner 0.1 pc around Sgr A\*, their presence has so far eluded detection. X-ray observations of our own galaxy and others may provide the first window to this interesting stellar population. In our own galaxy, Munro et al. (2005) have found an overabundance of X-ray sources in the vicinity of Sgr A\*, which seems to follow the underlying distribution of stars (Munro et al. 2006). For large distances, the X-ray sources appear to follow the BH distribution as well (FAK06). In other galaxies, many BHs may interact with the dense accretion disks around SMBHs, and in some circumstances be intrinsically more luminous than the SMBH (Deegan & Nayakshin 2007; Nayakshin & Sunyaev 2007).

The existence of a nuclear population of BHs may also be revealed through dynamical encounters with observable stars. Indeed, Weinberg et al. (2005) have shown that a decade of observations with the next generation of 30 m class telescopes may detect the scattering of the BHs with the so-called 'S-stars' that are within  $\approx 0.04$  pc of Sgr A\*. Microlensing by the BHs is expected to produce a much weaker signature (Miralda-Escudé & Gould 2000; Alexander & Loeb 2001; Chanamé et al. 2001). Strong encounters between the BHs and the same population of S-stars may dynamically eject the stars with high enough velocity to escape the potential of the galaxy (O'Leary & Loeb 2008) and populate the halo with the observed hyper-velocity stars (Brown et al. 2005, 2006). Strong encounters are also expected to tidally spin up long-lived stars, and so the BH population may be inferred through spectroscopic measurements of the spin of lower-mass stars (Alexander & Kumar 2001). Alternatively, one may infer the presence of the BHs by looking at density distribution of old pulsars (Chanamé & Gould 2002).

Finally, future GW observations with the space based

GW interferometer *LISA*<sup>3</sup> or the Earth-based second generation GW instruments are expected to detect the inspiral of such BHs into SMBHs (Gair et al. 2004; Rubbo et al. 2006; Hopman et al. 2007; Yunes et al. 2008) or IMBHs (Brown et al. 2007; Mandel et al. 2008), respectively, several times per year. Given the test particle limit of the BH, such encounters are expected to be a stringent test of General Relativity in the strong-field regime (Collins & Hughes 2004; Arun et al. 2006).

An interesting method for detecting a dense population of BHs is through the GWs they produce as they scatter on each other and get captured into a tight binary. Kocsis et al. (2006) estimated the expected detection rates of the first hyperbolic passage between such stellar mass black holes in globular clusters, and found rates to be typically less than  $0.1 \text{ yr}^{-1}$  for second generation GW instruments. Here, we consider the detectability of the much stronger GWs that follow once the eccentric binary has formed in galactic nuclei in this way and evolves toward coalescence. We explore this new method in § 3 and 4. However, in order to completely determine this rate we need to know how a multi-mass distribution of BHs relaxes around a SMBH in galactic nuclei. In the remainder of this section we calculate the steady-state distribution of BHs for a variety of models.

## 2.1 Fokker-Planck Equations

In our calculations, we follow the analysis of BW77, who derived the multi-mass Fokker-Planck equations for a spherically symmetric and isotropic distribution of stars around a SMBH,  $f_M(r, v) = f_M(E)$ , where  $E = (1/2)Mv^2 - GM_{\text{SMBH}}/r$  is the mechanical energy of bound orbits in the galactic cusp that are outside the loss cone (see below). Much of our analysis follows that of HA06, whose terminology we use throughout our calculations. The main difference in our work is that we look at a multi-mass distribution of BHs with slightly different initial conditions.

The SMBH determines the motion and dynamics of stars within its radius of influence,  $r_i = GM_{\text{SMBH}}/\sigma_*^2$ , where  $M_{\text{SMBH}}$  is the mass of the SMBH, and  $\sigma_*^2$  is the one-dimensional velocity dispersion of the underlying stellar population in the nucleus near the SMBH. For our calculations, we define a dimensionless time variable  $\tau = t/t_r$ , where  $t_r$  is the relaxation timescale at the radius of influence,

$$t_r = \frac{3(2\pi\beta_*/M_*)^{3/2}}{32\pi^2 G^2 M_*^2 n_* \ln \Lambda}, \quad (1)$$

where  $n_*$  is the number density of stars at  $r_i$  for the dominate population of stars of mass  $M_*$ ,  $\beta_* = M_*\sigma_*^2$ , and  $\ln \Lambda \approx \ln(M_{\text{SMBH}}/M_*)$  is the Coulomb logarithm. We also define a dimensionless unit of energy,  $x = -(M_*/M)(E/\beta_*)$ , and a dimensionless distribution function  $g_M(x) = [(2\pi\beta/M_*)^{3/2}n_*^{-1}]f_M(E)$ . In these units, the Fokker-Planck equation is (BW77,HA06)

$$\frac{\partial g_M(x, \tau)}{\partial \tau} = -x^{5/2} \frac{\partial}{\partial x} Q_M(x) - R_M(x), \quad (2)$$

<sup>3</sup> <http://www.lisa-science.org/>

where

$$Q_M(x) = \sum_m \frac{M}{M_*} \frac{m}{M_*} \int_{-\infty}^{x_D} dx' [\max(x, x')]^{-3/2} \times \left( g_M(x) \frac{\partial g_m(x')}{\partial x'} - \frac{m}{M} g_m(x') \frac{\partial g_M(x)}{\partial x} \right). \quad (3)$$

is the rate stars of mass  $M$  flow to energies larger than  $x$ , and  $R_M(x)$  is the rate stars are destroyed by the SMBH. We are interested in the distribution of BHs in the inner pc and therefore look only at the empty-loss cone regime. Thus, the angular momentum averaged destruction rate of stars of mass  $M$  with energy  $x$  is (HA06)

$$R_M(x) = \frac{g_M(x)}{\tau_r(x) \ln[J_c(x)/J_{LC}]}, \quad (4)$$

where  $\tau_r$  is the approximate local relaxation time at radius  $r = r_i/(2x)$ ,

$$\tau_r = \frac{M_*^2}{\sum_M g_M(x) M^2}, \quad (5)$$

$J_c(x) = GM_{\text{SMBH}} \sigma_*^{-1} (2x)^{-1/2}$  is the angular momentum of a circular orbit at a radius  $r = r_i/(2x)$ , and  $J_{LC}$  is the maximum angular momentum for the object to be destroyed or consumed by the SMBH. For stars  $J_{LC} = GM_{\text{SMBH}} \sigma_*^{-1} (2(x + x_{\text{td}}))^{1/2} x_{\text{td}}^{-1}$  corresponds to a star coming within tidal disruption radius of the SMBH, where  $x_{\text{td}} = (M_{\text{SMBH}}/M_*)^{-1/3} r_i/R_*$  and  $R_*$  is the radius of the star. BHs plunge into the SMBH when  $J < J_{LC} = 4GM_{\text{SMBH}}/c$ .

We numerically integrate Eq. (2) with our initial conditions given in § 2.2 until  $g_M(x)$  reaches a steady state for all  $M$ . For all of our runs this occurs before  $\tau = 1$ . A computationally straightforward simple iterative way to generate the steady state solution for Eq. (2) satisfying  $\frac{\partial g_M}{\partial \tau} \equiv 0$  is to follow the time evolution of the distribution from the initial conditions.

After the integration is complete, we calculate the number density of stars at radius  $r$ ,

$$n_M(r) = 2\pi^{-3/2} n_* \int_{-\infty}^{\phi(r)} dx g_M(x) (\phi(r) - x)^{1/2}, \quad (6)$$

where  $\phi(r)$  is the dimensionless specific potential. Until now, we have assumed that the stars were on entirely Keplerian orbits around the SMBH (i.e. that  $\phi(r) = r_i/r$ ). This assumption was necessary in order to simplify the Fokker-Planck equations to Eq. (2) (BW76). However, for our calculations in § 3, it is important that the BH density goes to zero as  $r$  approaches infinity. We therefore calculate  $\phi(r)$  and  $n_M(r)$  iteratively after calculating the steady-state distribution functions  $g_M(x)$ . We do this by sequentially solving for  $n_M(r)$  (Eq. 6) and

$$\phi(r) = \frac{r_i}{r} - \int_0^r \frac{M(< r) r_i}{M_{\text{SMBH}} r} dr \quad (7)$$

where  $M(< r) = \sum_M \int_0^r 4\pi r^2 n_M(r) dr$  is the total mass of stars interior to  $r$ , thus accounting for the stars’ contribution to the potential as well as the SMBH’s contribution. We find that we converge to a single solution for  $\phi(r)$  and  $n_M(r)$  before about 6 iterations. This solution to the number density and potential is fully consistent with the distribution functions  $g_M(x)$ . However, Equations 2 & 3 implicitly assume that, as  $r \rightarrow \infty$ , the potential approaches

zero and the number density approaches a constant. This assumption is approximately followed as long as the core radius of the isothermal sphere  $r_c = [9\sigma_*^2/(4\pi G\rho_0)]^{1/2}$  (Binney & Tremaine 1987) is larger than the radius of influence of the SMBH. We also note that the number density is the statistical average. In cases of the small numbers of BHs, we assume that values we determine will match the average over many galaxies. However, we caution that the dynamics of such systems will likely behave differently than assumed here.

## 2.2 Initial Conditions and BH Mass Distributions

The initial conditions of our models are described entirely by the distribution functions of unbound stars  $g_M(x < 0)$ . Sufficiently far from the radius of influence of the SMBH the population of visible stars appear to be similar to an isothermal sphere, with a constant velocity dispersion and a number density distribution that scales as  $\propto r^{-1.8}$  (Genzel et al. 2003; Schödel et al. 2007). We therefore set  $g_*(x) = \exp(x)$  for  $x < 0$ , which corresponds to an isothermal sphere of stars. We look at only one population of stars of mass  $M_* = 1 M_\odot$ . This is justified by previous analyses of mass segregation that show that the underlying stellar population, being considerably less massive than BHs, tends to follow the same distribution function independent of mass where the BHs dominate the relaxation (HA06, FAK06). We confirm this conclusion in § 2.3. Although there is a significant fraction of more massive stars in nuclei, their lifetimes are expected to be less than the relaxation timescale at most  $r$  and are in such small number that they should not contribute to the dynamics significantly.

We assume that the BHs initially follow the distribution of the stars, and amount to a total fraction,  $C_{\text{BH}} = \sum_M C_M$ , of the number density. BH natal kick velocities are expected to be much less than the velocity dispersions of the systems we are interested in (White & van Paradijs 1996; Willems et al. 2005), and so we expect the BHs’ velocity dispersion to be similar to the stars’. Therefore, we set  $g_M(x) = C_M \exp(x)$ , yielding a BH number density of  $C_M n_*$  near  $r_i$ . This is in contrast to the work of BW77 and HA06a, who both assume that the population of stars was already in thermal equipartition (i.e.  $M\beta_M = M_*\beta_*$ ). BW77 addressed the distribution of stars in globular clusters, which have half-mass relaxation times much shorter than the Hubble time and so the entire system should reach equipartition. In contrast, in galactic nuclei the relaxation timescale for large radii is usually longer than the age of the universe, and so the source population could not reach a complete equilibrium. HA06 made a numerical error in how they normalised the BH distribution and so had reasonable agreement between their work and previous works. However, with the proper normalisation, they would have found the number of BHs to be  $(M/M_*)^{3/2} = 10^{3/2}$  times larger than their results indicated. This is because in the case of a velocity dispersion independent of mass, the ratio of number densities of objects is described by  $n_M/n_* = C_M/C_*$ , whereas for a population in thermal equilibrium we get  $n_M/n_* = C_M M^{3/2}/(C_* M_*^{3/2})$ . Because the steady-state distribution function is most sensitive to  $g(0)$  and not the functional form  $g(x < 0)$ , their

results are similar to ours when one uses the incorrect normalisation.

One goal of our analysis is to see if the mass distribution of BHs may be determined either through dynamical interactions with their environment, or through the release of GWs. We therefore look at a variety of time-independent BH mass functions parametrised as power-laws. The models are determined by four basic parameters: the total number fraction of BHs,  $C_{\text{BH}} = \sum_M C_M$ ; the slope of the BH mass function,  $\beta$ , where  $dn_M/dM \propto M^{-\beta}$ ; the minimum BH mass,  $M_{\text{min}}$ ; and, finally, the maximum BH mass in the nucleus,  $M_{\text{max}}$ . In our calculations, we approximate the distribution of the BHs with  $N = 9$  discrete distribution functions with

$$C_i = \int_{M_{\text{min}+i\Delta M}^{M_{\text{min}}+(i+1)\Delta M}} \gamma M^{-\beta} dM, \quad (8)$$

where  $\Delta M = (M_{\text{max}} - M_{\text{min}})/N$ , and  $\gamma$  is normalised such that  $\sum_i C_i = C_{\text{BH}}$ . We set the mass for each distribution function to be the average mass for that bin,

$$M_i = \int_{M_{\text{min}+i\Delta M}^{M_{\text{min}}+(i+1)\Delta M}} (\gamma/C_i) M^{-\beta+1} dM. \quad (9)$$

We describe the numbers used above in detail below, and outline them in Table 1.

The number fraction of BHs in galactic nuclei is sensitive to the initial mass function (IMF) of high mass stars. For a Kroupa IMF (Kroupa & Weidner 2003) we estimate  $C_{\text{BH}} \approx 0.001$  by assuming that all stars with mass  $M > 20 M_{\odot}$  become BHs. A similar distribution of stars formed uniformly throughout time was found to be consistent with the K-band luminosity distribution of stars in the galactic centre (Alexander & Sternberg 1999). However, more recent observations of our Galactic Center suggest the IMF slope of high mass stars may be considerably shallower than those in regular clusters (see, e.g., Nayakshin & Sunyaev 2005; Nayakshin et al. 2006; Paumard et al. 2006; Maness et al. 2007). Paumard et al. (2006) found that the stars in an apparent disk around Sgr A\* are best fit with a flattened IMF  $\propto m^{-\beta_{\text{imf}}}$  with  $\beta_{\text{imf}} \approx 0.85 - 1.35$  and a depletion of low mass stars. This is consistent with the work of Nayakshin & Sunyaev (2005), who constrained the number of young low mass objects with X-ray observations, and determined there to be a deficiency of stars with mass  $\lesssim 3 M_{\odot}$ . Most recently, Maness et al. (2007) looked at late-type giants and concluded that the MF of high mass stars may be as shallow as  $\beta_{\text{imf}} \approx 0.85$ . A shallow MF is also expected theoretically (Morris 1993) and is consistent with the most recent hydrodynamic simulations of star formation in the Galactic Center (Alexander et al. 2008). Considering the abundant evidence for an alternative IMF in galactic nuclei, we therefore look at a wide range of number fractions, setting  $C_{\text{BH}} = 0.001, 0.01$ , and  $0.1$ , which roughly corresponds to  $\beta_{\text{imf}} = 2.3, 1.5$ , and  $0.8$  respectively.

The mass distribution of BHs is relatively unconstrained. Currently, the best constraints come from the couple of tens of X-ray binaries with dynamically determined BH masses (Remillard & McClintock 2006). Each measurement often has considerable uncertainty, but the masses seem to span a range of  $\sim 3 - 18 M_{\odot}$ . There is now strong dynamical evidence for BHs with even greater masses, up to  $23-34 M_{\odot}$ , in low metallicity environments (Orosz et al. 2007; Prestwich et al. 2007; Silverman & Filippenko 2008).

Nevertheless, these observations suffer from a severe observational bias; the BHs must be in a close binary to be observed. Theoretical estimates for the mass distribution are also highly uncertain. Belczynski et al. (2004) have used their sophisticated population synthesis models to determine the expected distribution of BH masses in a variety of environments. Typically, they expect most BHs in high metallicity environments to have a uniform distribution of masses between  $\sim 5 - 10 M_{\odot}$ , but do find that significantly more massive BHs may form from the merger of the BH with a high mass companion star. Unfortunately, these massive BHs would not be found in X-ray binaries, unless they were introduced into one dynamically. Given these uncertainties, we choose to parametrise the mass distribution of BHs as a power-law  $dn_M/dm \propto m^{-\beta}$ , where we consider  $\beta = 2$  and  $\beta = 3$ . We look at the importance of the highest mass BHs, by modelling different upper limits on BH mass,  $M_{\text{max}}$ . We also have a model based on the work of Belczynski et al. (2004). In Model BSR, we use a flat  $\beta = 0$  model of BHs with masses between  $5$  and  $10 M_{\odot}$  with a fraction  $\sim 0.01$  of BHs with mass  $25 M_{\odot}$ . This is consistent with their Model C2 of solar metallicity stars and based on their Figure 7.

For the remainder of § 2, we focus our results on Milky Way like nuclei, and assume that  $M_{\text{SMBH}} = 3.5 \times 10^6 M_{\odot}$  (Ghez et al. 2005; Eisenhauer et al. 2005) and that the velocity dispersion of the stars and stellar BHs is  $\sigma_* = 75 \text{ km s}^{-1}$  (HA06). In § 3 we also consider other galaxies that have relaxation times short enough to reach steady state in a Hubble time with  $M_{\text{SMBH}} \sim 10^4 - 10^7 M_{\odot}$ , in order to calculate the overall rate of GWs sources in the universe.

### 2.3 Results and Implications

For all of our models, independent of the BH mass function (namely,  $\beta$ , and the mass range of BHs), the most massive BHs always become the dominant BH species in the inner  $\sim 0.1 \text{ pc}$  of the galactic nucleus. In Figure 1, we plot the number density of the stars and BHs as a function of radius. As has been found previously (BW77, HA06, FAK06), deep in the Keplerian potential of the SMBH, the distribution functions of the stars and BHs become power-laws of the negative specific energy of the objects  $g_m(x) \propto x^{p_m}$ , and hence have a power-law density profile  $\propto r^{-3/2-p_m}$ . We find that throughout all of our simulations, the exponent  $p_m$  is best fit by a linear relationship between the mass ratio of the object,  $m$ , and the most massive BH,  $M_{\text{max}}$ ,

$$p_m = p_0 \frac{m}{M_{\text{max}}}, \quad (10)$$

where  $p_0 \approx 0.5 - 0.6$ . We have found that  $p_0$  usually has a small scatter ( $\sim 20\%$ ), depending on  $M_{\text{max}}$  and  $\beta$ ; however, given  $p_0$ , Eq. (10) is often accurate to  $\lesssim 1\%$ . This relationship is similar to that found in BW77, who found that  $p_0 \approx 0.25 - 0.3$ , when they looked at two different components with comparable number densities. Alexander & Hopman (2008) attributes the steeper density profiles to “strong” mass segregation, where the relaxation of the system is determined by the many low mass objects. In their calculations,  $p_0$  increases monotonically with  $M_{\text{max}}$ , however the rate at which it increases is rather slow after  $p_0 \sim 0.5$ . In contrast, in our simulations with a mass spectrum of massive objects and accounting for the loss-cone, we do not find

**Table 1.** BH Models and Results. Unless otherwise noted, these results apply to a Milky Way like galaxy with  $M_{\text{SMBH}} = 3.5 \times 10^6 M_{\odot}$ ,  $\sigma_* = 75 \text{ km s}^{-1}$  and  $r_i = GM_{\text{SMBH}}/\sigma_*^2 = 2.7 \text{ pc}$ . The columns are, from left to right, (1) the model name, (2) the slope of the BH mass function, (3) the minimum BH mass, (4) the maximum BH mass, (5) the fraction of stars that are BHs, (6) the merger rate of GW capture binaries per model galaxy, and (7) the expected AdLIGO detection rate as calculated in § 4.

Model	$\beta$	$M_{\text{min}}$ ( $M_{\odot}$ )	$M_{\text{max}}$ ( $M_{\odot}$ )	$n_{\text{BH}}/n_*$	Merger Rate per Galaxy ( $\text{yr}^{-1}$ )	AdLIGO Detection Rate ( $\xi_{30\text{yr}^{-1}}$ )
A	2	5	10	0.001	$2.2 \times 10^{-10}$	5.8
A $\beta$ 3	3	5	10	0.001	$2.0 \times 10^{-10}$	5.2
B	2	5	15	0.001	$2.8 \times 10^{-10}$	16
B $\beta$ 3	3	5	15	0.001	$2.5 \times 10^{-10}$	13
B-1	2	5	15	0.1	$5.3 \times 10^{-9}$	220
B-2	2	5	15	0.01	$8.3 \times 10^{-10}$	40
Be5 <sup>a</sup>	2	5	15	0.001	$2.8 \times 10^{-10}$	15
C	2	5	25	0.001	$3.8 \times 10^{-10}$	46
D	2	10	15	0.001	$3.4 \times 10^{-10}$	23
E	2	10	25	0.001	$3.2 \times 10^{-10}$	12
E-1	2	10	25	0.1	$1.2 \times 10^{-8}$	1200
E-2	2	10	25	0.01	$1.3 \times 10^{-9}$	150
F-1	2	10	45	0.1	$1.5 \times 10^{-8}$	2700
BSR <sup>b</sup>	0	5	10	0.001	$2.9 \times 10^{-10}$	43

<sup>a</sup> This is evaluated for a SMBH with  $M_{\text{SMBH}} = 1 \times 10^5 M_{\odot}$  and  $\sigma_* = 30 \text{ km s}^{-1}$ .

<sup>b</sup> There is an additional population of  $25 M_{\odot}$  BHs with  $n_{\text{bh}}/n_* = 10^{-5}$

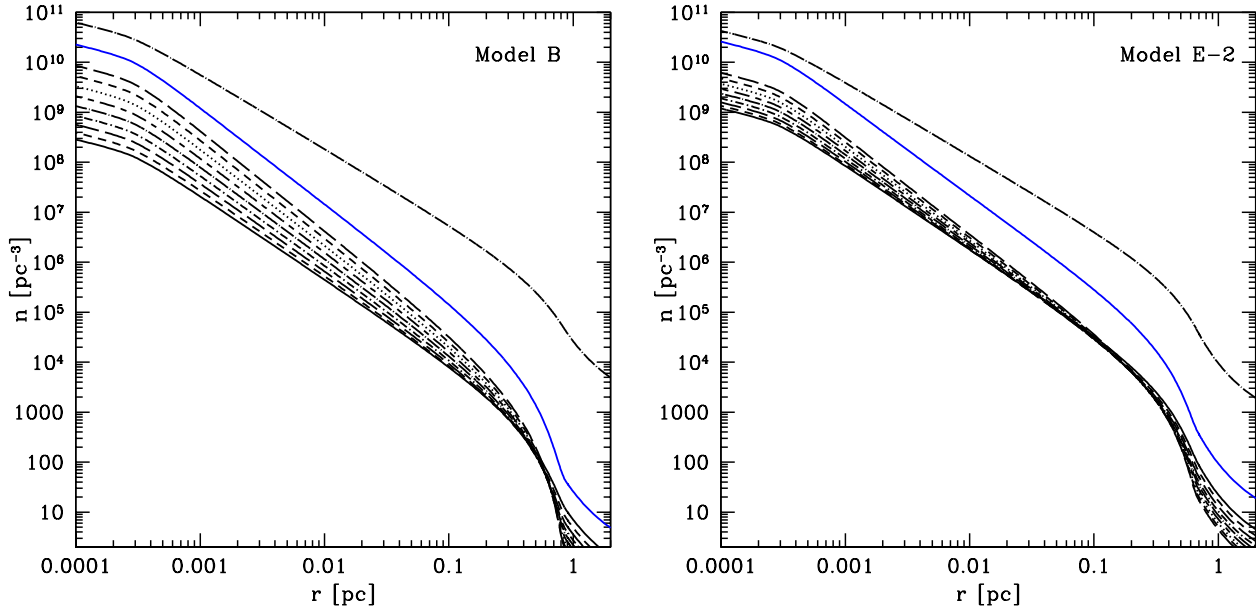


**Figure 1.** The number density of stars and BHs for Model B (left) and E-2 (right). The top dash-dotted line is the number density of the stars as a function of radius. The alternating dotted and dash-dotted lines show the number density of the separate mass bins used in our calculations with the most massive BHs having the largest number density interior to  $r \approx 0.3 - 0.6 \text{ pc}$ . The solid blue line is the total BH number density  $= \sum_M n_M(r)$ . Near  $r \approx 1 \text{ pc}$  the potential of the stars and BHs is equal to the Keplerian potential of the SMBH. The rapid drop in the number of BHs drops rapidly here because of the rigid boundary condition at  $\phi = 0$ . In all of our simulations, the bin of the most massive BHs dominates the number density of BHs in the inner  $\sim 0.1 \text{ pc}$ .

that the maximum power-law index  $p_0$  to depend sensitively on the number or mass of the highest mass objects. However, we have not looked at the large range of parameters of Alexander & Hopman (2008).

Mass segregation in galactic nuclei ceases when the BHs

begin to dominate the relaxation process in the inner cusp. Typically, this is expected when  $n_{\text{BH}} M_{\text{BH}}^2 > n_* M_*^2$ . One therefore may try to detect the presence of a cluster of BHs through their interactions with the luminous stars in its vicinity. We can estimate the relaxation timescale at a radius

$r$  from Eqs. (1) & (5), in terms of the Keplerian potential of the SMBH

$$t_r(r) = \frac{3(2\pi v_c^2(r))^{3/2}}{32\pi^2 G^2 \ln \Lambda \sum_M M_M^2 n_M(r)} \quad (11)$$

where  $v_c(r) = \sqrt{GM_{\text{SMBH}}/r}$  is the circular velocity around the SMBH at radius  $r$ . In Figure 2, we have plotted the relaxation timescale as a function of radius for Models B and E-2. The BHs begin to dominate the local relaxation processes at  $r \sim 0.5$  pc, consistent with the results of FAK06 and HA06. We find that the relaxation timescale in the galactic centre is highly sensitive to the assumed mass distribution of the BHs, since the lower density of the BHs is easily outweighed by their greater mass. By finding a tracer of the relaxation time in the inner 0.1 pc of the galactic centre, it may be possible to determine if such heavy BHs even exist in our galaxy (Chanamé & Gould 2002).

As discussed above, a population of massive BHs in the galactic centre may be revealed through strong encounters with their neighbouring stars. Because the BHs are more massive than the typical star, they tend to drive stars out of the nucleus, creating a shallow stellar density profile (FAK06; HA06; for observations see Genzel et al. 2003 and more recently Schödel et al. 2007). Miralda-Escudé & Gould (2000) proposed that a population of such BHs may be seen through stars on very radial orbits that are ejected by close encounters by the BHs. In some extreme encounters, O’Leary & Loeb (2008) showed that strong interactions between BHs and stars can lead to the stars being ejected from the Milky Way altogether as the observed hypervelocity stars (Brown et al. 2005, 2006). The results of O’Leary & Loeb (2008) were sensitive to the assumed BH mass distribution. Self-segregation of the BHs is an important consideration when evaluating the likelihood of the scenario, and the velocities of ejected HVSS (Sesana et al. 2007).

As a more extreme example of a strong encounter, BHs and stars may physically collide into each other (Morris 1993, FAK06) producing strong X-ray and UV flares in galactic nuclei. Interestingly, we find that the total rate of physical collisions between stars and BHs can be comparable to the rate stars are tidally disrupted by the SMBH, and may be visible in variability surveys of galactic nuclei. Such encounters may have smaller bolometric luminosities than stars disrupted by the SMBH due to their lower Eddington luminosity.

### 3 BINARY FORMATION, INSPIRAL, AND EVENT RATES

When two compact objects have a close encounter, they can emit sufficient energy through GWs that they become bound and form a binary. To see the importance of such a process in galactic nuclei, we first estimate the rate of binary formation for two typical  $10 M_\odot$  BHs. We present more detailed calculations later in this section. To first order, two BHs with an initial relative velocity  $w$  will form a bound binary due to the emission of GWs if they come within a distance  $\approx 7.4 \times 10^{-3} R_\odot (w/100 \text{ km s}^{-1})^{-4/7}$  at closest approach (see Eq. [18] below). This corresponds to an initial impact parameter (the distance of closest approach if the BHs moved in

straight lines) of (Eq. [17])  $b \lesssim 2.4 R_\odot (w/100 \text{ km s}^{-1})^{-9/7}$ . We expect that a single BH will undergo such an encounter approximately every  $(\pi b^2 n_{\text{BH}} w)^{-1} = 3.4 \times 10^{12} (n_{\text{BH}}/10^6 \text{ pc}^{-3})^{-1} (w/100 \text{ km s}^{-1})^{11/7} \text{ yr}$ . The total rate of binary formation is then approximately (see, e.g., Eq. [31])  $\int n_{\text{BH}}^2 \pi b^2 w 4\pi r^2 dr$ , where  $v(r) \sim v_c(r) = \sqrt{GM_{\text{SMBH}}/r}$  is the Keplerian circular velocity at radius  $r$ . Integrating from  $r = 10^{-3}$  pc to  $r = 1$  pc, yields a rate of  $3.4 \times 10^{-10} \text{ yr}^{-1} [N_{\text{BH}}/(2 \times 10^4)]^2$  for  $N_{\text{BH}}$  BHs in a density cusp around the SMBH with  $n_{\text{BH}} \propto r^{-2}$ . This is in good agreement with our more detailed calculations presented in § 3.2.

In this section, we calculate the formation rate of such gravitational wave capture binaries in greater detail. We first calculate the conditions necessary to form gravitational wave capture binaries and the properties of their eventual inspiral in different environments. We then calculate the rate of binary formation for the multi-mass, segregated clusters of BHs that we modelled in § 2. Finally, we extrapolate our results for galactic models, including the distribution of SMBHs in the universe and accounting for the statistical variance in the number density of stars surrounding the SMBHs, in order to estimate the comoving rate density of binary formation and inspiral.

In our calculations, we express our equations with the symmetric mass ratio of the encounter  $\eta = (mM)/(m+M)^2$ , and total mass of the BHs  $M_{\text{tot}}$ . With these variables, the reduced mass is  $\mu = M_{\text{tot}}\eta$ .

#### 3.1 Orbital Evolution

In the following sections, we shall work with dimensionless parameters in units  $G = c = 1$ , where the total mass  $M_{\text{tot}}$  has length and time dimensions. We define the dimensionless pericenter distance as  $\rho_p = r_p/M_{\text{tot}}$ , dimensionless semimajor axis for an eccentric orbit with eccentricity  $e$  as  $\alpha \equiv a/M_{\text{tot}} = \rho_p/(1-e)$ . In these units, the mean orbital angular frequency from Kepler’s law is simply  $\omega_{\text{orb}} = M_{\text{tot}}^{-1} \alpha^{-3/2} = \rho_p^{-3/2} (1-e)^{3/2}$ , the angular frequency at pericenter passage is  $\omega_p = M_{\text{tot}}^{-1} \rho_p^{-3/2} (1+e)^{1/2}$ , the orbital time is  $\Delta t_{\text{orb}} \equiv f_{\text{orb}}^{-1} \equiv 2\pi\omega_{\text{orb}}^{-1}$ . We define the characteristic time of pericenter passage as  $\Delta t_p \equiv f_p^{-1} \equiv 2\pi\omega_p^{-1}$ , which satisfies  $\Delta t_p = \Delta t_{\text{orb}}$  for circular encounters, but is much smaller for eccentric encounters.

##### 3.1.1 First Passage, Formation of Binaries

Two BHs of mass  $m$  and  $M$  will form a binary if they undergo a close encounter and release enough energy to become bound,  $\delta E > \eta M_{\text{tot}} w^2/2$ , where  $w = |\mathbf{v}_m - \mathbf{v}_M|$  is the magnitude of relative velocity of the BHs at infinity, and we ignore the presence of the SMBH during the encounter and assume that the interaction is local. Given the relativistic nature of such events, and the comparatively low velocity dispersions in nuclei, the encounters are always nearly parabolic (Quinlan & Shapiro 1987; Lee 1993). In this limit, the amount of energy released during the encounter is (Peters & Mathews 1963; Turner 1977)

$$\delta E \approx -\frac{85\pi}{12\sqrt{2}} \frac{\eta^2 M_{\text{tot}}^{9/2}}{r_p^{7/2}}, \quad (12)$$

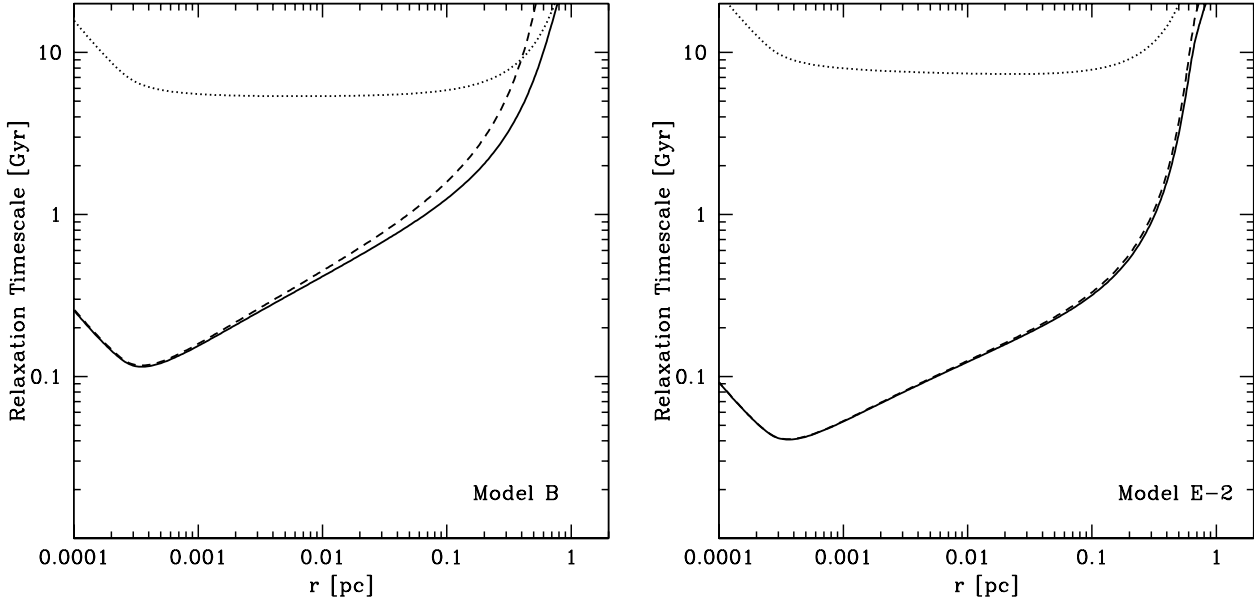


**Figure 2.** The relaxation timescale as a function of radius for Model B (left) and E-2 (right) plotted in Gyr. The solid line shows the relaxation timescale for the entire system. The long dashed and dotted lines show the contribution of the BHs and stars respectively. Although the stars contribute to the formation of the cusp and are the most common objects in the system, their low mass precludes them from dominating the relaxation in the inner  $\approx 0.6$  pc of the cusp. The break in the relaxation time at  $\sim 0.0002$  pc is due to our boundary condition that no stars have  $x > 10^4$ .

where  $r_p$  is the distance of closest approach,

$$r_p = \left( \sqrt{\frac{1}{b^2} + \frac{M_{\text{tot}}^2}{b^4 w^4}} + \frac{M_{\text{tot}}}{b^2 w^2} \right)^{-1} \approx \frac{b^2 w^2}{2M_{\text{tot}}} \left( 1 - \frac{b^2 w^4}{4M_{\text{tot}}^2} \right) \quad (13)$$

and  $b$  is the impact parameter of the encounter, and in the second line we have expanded to first order in  $w/c$ .

The final properties of the system are determined by the system’s final energy,  $E_{\text{final}} = M_{\text{tot}}\eta w^2/2 + \delta E$ , and angular momentum,  $L_{\text{final}} = M_{\text{tot}}\eta b w + \delta L$ , where

$$\delta L \approx -\frac{6\pi M_{\text{tot}}^4 \eta^2}{r_p^2}, \quad (14)$$

is the amount of angular momentum lost in GWs (Peters 1964). For nearly all of the encounters we find  $|\delta L| \ll M_{\text{tot}}\eta b w$  and so we set  $\delta L = 0$ . If the total energy of the system is negative,  $E_{\text{final}} < 0$ , then the system will remain bound with a semi-major axis,

$$a_0 = -\frac{M_{\text{tot}}^2 \eta}{2E_{\text{final}}}, \quad (15)$$

eccentricity,

$$e_0 = \sqrt{1 + 2\frac{E_{\text{final}} b^2 w^2}{M_{\text{tot}}^3 \eta}}, \quad (16)$$

and pericenter,  $r_{p0} = a_0(1 - e_0)$ .

With the criterion  $E_{\text{final}} < 0$  for binary formation, the maximum impact parameter for two BHs with relative ve-

locity  $w$  to become bound is

$$b_{\text{max}} = \left( \frac{340\pi}{3} \right)^{1/7} M_{\text{tot}} \frac{\eta^{1/7}}{w^{9/7}}. \quad (17)$$

Substituting in Eq. (13), this corresponds to a maximum pericenter distance

$$r_{p,\text{max}} = \left( \frac{85\pi}{6\sqrt{2}} \right)^{2/7} M_{\text{tot}} \frac{\eta^{2/7}}{w^{4/7}} \times \left( 1 - \frac{1}{4} \left( \frac{85\pi}{3} \right)^{2/7} (4\eta)^{2/7} w^{10/7} \right). \quad (18)$$

We shall demonstrate below that event rates are dominated by the central regions of the galactic cusp. For  $m = M$  ( $\eta = 1/4$ ) and  $w = 1000 \text{ km s}^{-1}$ ,  $b_{\text{max}} \approx 2900 M_{\text{tot}}$ , and  $r_{p,\text{max}} = 47 M_{\text{tot}}$ . The correction in Eq. (18) is clearly negligible for nonrelativistic initial conditions.

### 3.1.2 Eccentric Inspiral

After the binary forms with dimensionless pericenter distance  $\rho_{p0} = r_{p0}/M_{\text{tot}}$  and eccentricity  $e_0$ , its orbit will decay through the emission of GWs (Peters 1964),

$$\frac{d\rho_p}{dt} = -\frac{64}{5} \frac{M_{\text{tot}}^{-1} \eta^2}{\rho_p^3} \frac{(1-e)^{1/2}}{(1+e)^{7/2}} \left( 1 + \frac{73}{24} e^2 + \frac{37}{96} e^4 \right) \quad (19)$$

$$\frac{de}{dt} = -\frac{304}{15} \frac{M_{\text{tot}}^{-1} \eta}{\rho_p^4} e \frac{(1-e)^{3/2}}{(1+e)^{5/2}} \left( 1 + \frac{121}{304} e^2 \right) \quad (20)$$

where we assume  $\rho_p = r_p/M_{\text{tot}} = a/[M_{\text{tot}}(1-e)]$  until the last stable orbit.

We evolve the orbits following Peters (1964) for the evolution of the dimensionless periapsis  $\rho_p$ , the time-to-merger,

$t$ , as a function of the instantaneous eccentricity,  $e$ . Note that if starting from a parabolic passage, the initial condition for the orbit is determined from exactly one parameter,  $\rho_{p0}$ . Dividing Eq. (19) with Eq. (20) yields a separable differential equation for  $\rho_p(e)$ . The solution satisfying a parabolic encounter initial condition  $\rho_p = \rho_{p0}$  at  $e = 1$  is

$$\rho_p(\rho_{p0}, e) = \rho_{p0} \kappa_\rho(e) \quad (21)$$

where

$$\kappa_\rho(e) = 2 \left( \frac{304}{425} \right)^{\frac{870}{2299}} e^{\frac{12}{19}} \left( 1 + \frac{121}{304} e^2 \right)^{\frac{870}{2299}} (1+e)^{-1} \quad (22)$$

for which  $\kappa_\rho = 1$  at  $e = 1$ . The orbital evolution equations (21) & (22) are valid far from the horizon  $\rho_p \gg 2$ . Once the last stable orbit (LSO) is reached the evolution is no longer quasiperiodic and the binary quickly coalesces. In the leading order ratio approximation for infinite mass ratio and zero spins,

$$\rho_p(e_{\text{LSO}}) = \frac{6 + 2e_{\text{LSO}}}{1 + e_{\text{LSO}}}, \quad (23)$$

which we solve numerically for  $e_{\text{LSO}}(\rho_{p0})$  using Eqs. (21) & (22).

The time evolution of the eccentricity can be written using Eqs. (19) & (20) as

$$t_{\text{mg}}(e) = \frac{15}{19} \left( \frac{304}{425} \right)^{\frac{3480}{2299}} M_{\text{tot}} \eta^{-1} \rho_{p0}^4 \times \int_0^e \epsilon^{\frac{29}{19}} \frac{\left( 1 + \frac{121}{304} \epsilon^2 \right)^{\frac{1181}{2299}}}{(1 - \epsilon^2)^{3/2}} d\epsilon \quad (24)$$

where  $t_{\text{mg}}(e)$  denotes the time remaining until coalescence when the eccentricity is  $e$ . Close to coalescence this is approximately,

$$t_{\text{mg}}(e) \approx \frac{5}{16} \left( \frac{304}{425} \right)^{\frac{3480}{2299}} M_{\text{tot}} \eta^{-1} \rho_{p0}^4 e^{\frac{48}{19}} \quad \text{if } e \ll 1. \quad (25)$$

while the total merger time starting from a highly eccentric initial orbit (Peters 1964)

$$t_{\text{mg}} \approx \frac{3}{85} \frac{a^4}{M_{\text{tot}}^3 \eta} (1 - e^2)^{7/2} \quad \text{if } e \approx 1. \quad (26)$$

Substituting Eqs. (15) & (16) for the initial separation and eccentricity  $a_0$  and  $e_0$  into Eq. (26) we get,

$$t_{\text{mg}} \approx \frac{3\sqrt{3}}{170\sqrt{85}\pi} \frac{(bw)^{21/2}}{M_{\text{tot}}^{19/2} \eta^{3/2}} \quad (27)$$

where we have set  $E_{\text{final}} = \delta E$ , ignoring the initial energy of the binary. This is an excellent approximation all the way out to  $0.99b_{\text{max}}$  because of the strong dependence of  $t_{\text{merge}}$  on the initial velocity  $w$ . The merger time reaches its maximum at  $b = b_{\text{max}}$  and simplifies to  $4\pi G M_{\text{tot}} / w^3$ : about two times the orbital period of a binary with circular velocity  $w$ .

For the most relevant systems, we find that such binaries will merge before they have a close encounter with a third body. The binary can be disrupted if it encounters a third body with a closest approach  $\lesssim 2a$  before it merges. For the maximum impact parameter to form a binary,  $b_{\text{max}}$ , the separation of the binary that forms is  $a \approx G M_{\text{tot}} / w^2$ . The typical timescale for an encounter to disrupt the binary

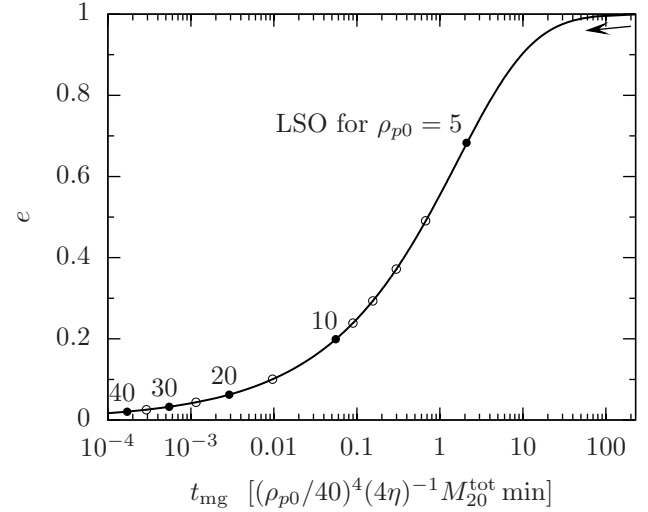


**Figure 3.** The eccentricity evolution as a function of time to merger. All of the orbits start off near  $e = 1$ , and depending on the initial periapsis  $\rho_{p0}$ , LSO corresponds to the eccentricity  $e_{\text{LSO}}$  shown with filled circles as marked. Open circles give  $e_{\text{LSO}}$  for equidistant intermediate values for  $\rho_{p0}$ . The curves should not be extrapolated to  $e < e_{\text{LSO}}$  as the evolution might be very different during the BH merger.

is  $\sim (12\pi a^2 n w)^{-1} = w^3 / (12\pi G^2 M_{\text{tot}}^2 n)$ , where the additional factor of 3 comes from gravitational focusing. Because of the strong dependence Eq. (27) has on the impact parameter ( $\propto b^{21/2}$ ), for any reasonable disruption timescale, a slightly closer impact will always compensate and allow the binary to merge before being disrupted. In fact, in order for the disruption timescale to be comparable to merger timescale, the number density of stars must be  $n \gtrsim 10^{15} \text{ pc}^{-3}$  for  $w = 100 \text{ km s}^{-1}$ . Because every binary results in a rapid merger, the rate of inspiral at any time is well approximated by the rate of binary formation.

Equation (24) provides an explicit monotonic relation between time and eccentricity. This relation is sensitive to the free parameters  $M_{\text{tot}}$ ,  $\eta$ , and  $\rho_{p0}$  only through the overall scaling  $M_{\text{tot}} \eta^{-1} \rho_{p0}^4$ . Therefore eccentricity can be thought of as a dimensionless time variable. Figure 3 illustrates the conversion between  $t$  and  $e$ . For the parameters,  $\rho_{p0} = 40$ ,  $M_{\text{tot}} = 20 M_{\odot}$ , and  $\eta = 0.25$ , the characteristic timescale is several hours for moderate–large eccentricities, and minutes for the final small eccentricity inspiral.

### 3.2 Event Rates

Given the cross-section for binary formation ( $\sigma_{\text{cs}} = \pi b_{\text{max}}^2$ ), we can now calculate the expected rate of binary formation in a single galactic nucleus,  $\Gamma_{\text{IGN}}$ . In order to evaluate the total contribution of different BH masses, ( $m, M$ ), velocities, ( $\mathbf{v}_m, \mathbf{v}_M$ ), and spatial position,  $r$ , within a single galactic nucleus, we need to integrate the differential rate  $d^9 \Gamma_{\text{IGN}} = \sigma_{\text{cs}} w f_m(r, \mathbf{v}_m) f_M(r, \mathbf{v}_M)$  over the corresponding distributions. Here  $w = |\mathbf{v}_m - \mathbf{v}_M|$  is still the magnitude of relative velocity between the BHs, and  $f_m$  and  $f_M$  are the 6-dimensional distribution functions of the BHs with mass  $m$  and  $M$  derived in § 2. Generally, this calculation requires

us to evaluate an integral over 9 variables,

$$\Gamma_{1\text{GN}} = \int_{r_{\min}}^{r_{\max}} dr 4\pi r^2 \int_{M_{\min}}^{M_{\max}} dM \int_{M_{\min}}^M dm \quad (28)$$

$$\iint_{x_m, x_M > 10, J > J_{\text{LC}}} d^3 v_m d^3 v_M f_m(r, \mathbf{v}_m) f_M(r, \mathbf{v}_M) \sigma_{\text{cs}} w,$$

where the integration bounds are set consistent with the distribution domains (see §2). The multi-dimensional integration can be greatly simplified to only three variables using a few approximations. First in §2.3, we assumed that the velocity distributions were isotropic. For fixed  $m$  and  $M$ , we switch integration variables from  $(\mathbf{v}_m, \mathbf{v}_M)$  to  $(\mathbf{v}_m - \mathbf{v}_M, \mathbf{v}_m + \mathbf{v}_M)$ , and adopt spherical coordinates. Since the integrand only depends on  $w$ , we can evaluate the integrals over the other 5 velocity components<sup>4</sup>

$$\int d^3 v_m \int d^3 v_M f_m(r, \mathbf{v}_m) f_M(r, \mathbf{v}_M) \sigma_{\text{cs}} w =$$

$$= n_m(r) n_M(r) \int dw \psi_{mM}(r, w) \sigma_{\text{cs}} w, \quad (29)$$

where  $\psi_{mM}(r, w)$  is the relative velocity distribution which can be expressed as a one-dimensional integral using the Dirac- $\delta$  function for a power-law dimensionless energy distribution profile  $g_m(x) \propto x^{p_m}$  (see §2 for a definition). Note that the phase space distribution functions of the BHs and stars are well approximated by a power-law  $g_m \propto x^{p_m}$  for  $x > 10$ .

We have numerically integrated the remaining velocity integral over the possible range of  $w$  for a variety of different slopes  $p_m$  and  $p_M$  and find that to within  $\lesssim 10\%$  the integrand is independent of the shape of the relative velocity distribution and only depends on the expected value of the relative velocities, and can be expressed with the expected value of the individual velocity magnitudes as

$$\int dw \psi_{mM}(r, w) \sigma_{\text{cs}} w \approx \pi b_{\max}^2 v_c(r), \quad (30)$$

where  $b_{\max}^2$  is evaluated at  $w = v_c(r)$  using Eq. (17), and  $n_m(r) \propto r^{-p_m - 3/2}$ . This is to be expected, since the encounters are practically parabolic such that the initial velocity profile is negligible compared to the velocity at periastron. Thus, Eq. (28) simplifies to

$$\frac{d^3 \Gamma_{1\text{GN}}}{dr dm dM} = 4\pi^2 b_{\max}^2 v_c(r) n_m(r) n_M(r) r^2, \quad (31)$$

so that the total rate in one galactic nucleus is

$$\Gamma_{1\text{GN}} = \int_{r_{\min}}^{r_{\max}} dr \int_{M_{\min}}^{M_{\max}} dM \int_{M_{\min}}^M dm \frac{d^3 \Gamma_{1\text{GN}}}{dr dm dM}. \quad (32)$$

In practice, we calculate  $\Gamma$  for all of our simulations by calculating  $n_m(r)$  and  $n_M(r)$  for discreet masses and sum over  $m < M$ .

<sup>4</sup> Some difficulties arise because of the integration bounds depend on the other parameters. However, the integrals can be evaluated under the approximation  $r_{\min} \leq r \leq r_{\max}$  and  $0 \leq v \leq v_{\text{esc}}(r)$ , where  $r_{\min}$  and  $r_{\max}$  are the minimum and maximum radii for a relaxed population of BHs in the nucleus and  $v_{\text{esc}}(r)$  is the escape velocity at radius  $r$ .

### 3.3 Results and Discussion

The resulting event rates integrated over a single galactic nucleus are presented in the sixth column of Table 1 for all of our model nuclei. The estimated rates vary between  $\sim 10^{-8}$ – $10^{-10} \text{ yr}^{-1}$  over the various models. We discuss the primary sources of uncertainties and other important aspects related to the event rates in detail below.

#### 3.3.1 Number of Black Holes

Overall, we find that the merger rate is most sensitive to  $C_{\text{BH}} = n_{\text{BH}}/n_*$ , however, the accretion of BHs by the SMBH reduces the naïve scaling relation  $\propto C_{\text{BH}}^2$ . Thus, as the number fraction of BHs increases by a factor of 100, the rate of mergers only increases by a factor of 20. The merger rate depends far less so on  $M_{\max}$  and  $M_{\min}$ , since, for larger  $M_{\max}$  the total number of BHs tends to be reduced in the inner  $\sim 0.1$  pc of the SMBH. The rate, however, remains relatively unchanged since the cross-section for binary capture increases with the BH mass.

#### 3.3.2 Pericenter Distance Dependence

For parabolic encounters, the differential of pericenter distances that lead to binary formation, according to Eq. (13) is to leading order

$$dr_p \approx \frac{w^2 b db}{M_{\text{tot}}}, \quad (33)$$

where we have fixed  $w$ , the relative velocity at infinity. Since  $d\Gamma/db \propto b \propto dr_p/db$ , the pericenter distribution that lead to binary capture ( $d\Gamma/dr_p$ ) is uniform out to a maximum pericenter distance  $r_{p\text{max}}$ . We can calculate the overall distribution of encounters that form binaries by changing the order of integration of Eq. (28) and leaving it as a function of  $r_p$ ,

$$\frac{d\Gamma_{1\text{GN}}}{dr_p} = \iiint \int dr dw dm dM 4\pi r^2 n_M(r) n_m(r)$$

$$\times \frac{M_{\text{tot}}}{w^2} w \psi_{mM}(r, w), \quad (34)$$

where  $\psi_{mM}(r, w)$  is the distribution function of relative velocities given by Eq. (29). The limits of the integration determine the functional form in three main regimes. For  $r_p < r_{p\text{max}}[w_{\max}(r_{\min})]$  where  $w_{\max}(r) = 2v_{\text{esc}}(r) = 2\sqrt{2}v_c(r)$  is the maximum relative velocity at radius  $r$ ,  $v_{\text{esc}}$  is the escape velocity, and  $r_{p\text{max}}(w)$  is defined in Eq. (18), Eq. (34) is independent of  $r_p$  and is integrated over the bounds

$$0 < w < w_{\max}(r)$$

$$r_{\min} < r < r_{\max}. \quad (35)$$

For  $r_{p\text{max}}(w_{\max}(r_{\min})) < r_p < r_{p\text{max}}(w_{\max}(r_{\max}))$  the limits of integration are determined by  $w_{\text{eq}}(r_p)$ , the inverse of Eq. (18) and  $r_{\text{eq}}(r_p) = 2GM_{\text{SMBH}}/w_{\text{eq}}(r_p)^2$ . In this regime, the limits of integration are split into two regions

$$0 < w < w_{\text{eq}}(r_p)$$

$$r_{\min} < r < r_{\text{eq}}(r_p), \quad (36)$$

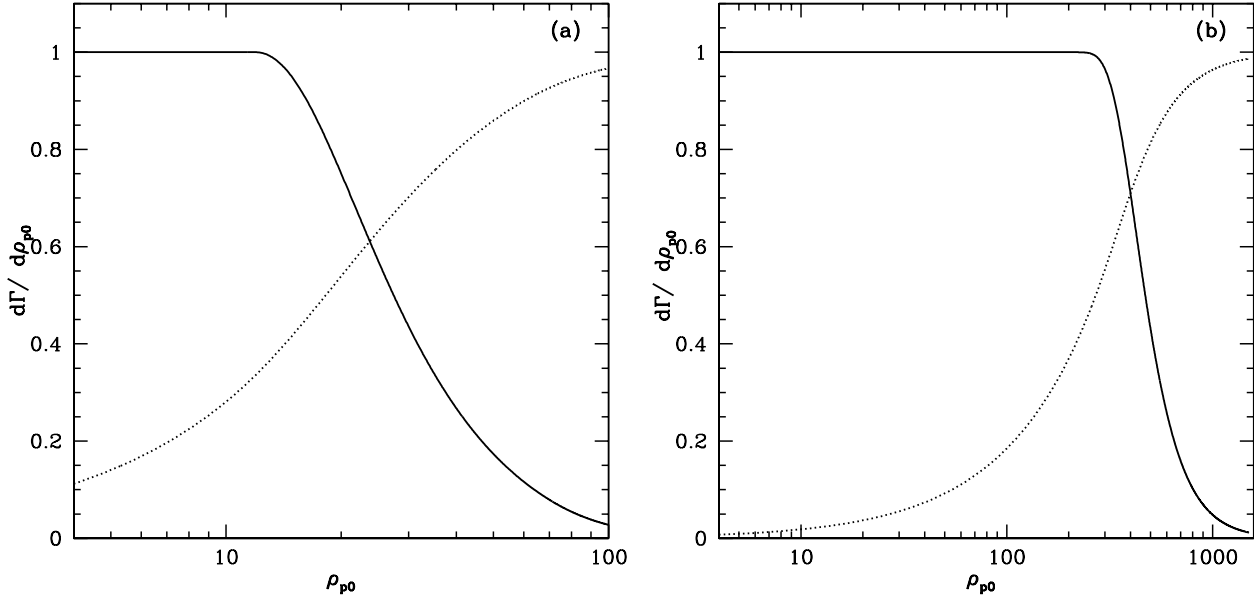


**Figure 4.** Normalised probability distribution and integrated probability distribution of initial pericenter distances for binaries in galactic nuclei (a) and in Spitzer-unstable massive star clusters without a central massive black hole (b; see § 3.3.6 for details). To calculate the values in this figure, we have assumed that the merger rate is dominated by the  $10 M_{\odot}$  BHs with a near Maxwellian velocity dispersion, and in galactic nuclei they have density profiles  $\propto r^{-2}$ , consistent with the density profile of the most massive objects in the nucleus (see § 2.3). The solid line is the differential rate of binary formation  $d\Gamma/dr_p$  and the dotted line represents the integrated probability  $\Gamma(r > r_p)$ . For galactic nuclei, the probability distribution is perfectly uniform out to pericenter distance  $r_{p \max}(w_{\max}, .001 \text{ pc}) \approx 12 M_{\text{tot}}$ , after which it drops off quickly. For globular clusters without a central massive BH the distribution is uniform out to  $r_p \approx 250 M_{\text{tot}}$ , and it begins to drop off as a Gaussian profile for  $r_p \gtrsim 540 M_{\text{tot}}$ .

and

$$\begin{aligned} w_{\text{eq}}(r_p) < w < w_{\text{max}}(r) \\ r_{\text{eq}}(r_p) < r < r_{\text{max}}. \end{aligned} \quad (37)$$

Finally, for  $r_p > r_{p \max}(2\sqrt{2}v_c(r_{\text{max}}))$  the limits of integration are

$$\begin{aligned} 0 < w < w_{\text{eq}}(r_p) \\ r_{\text{min}} < r < r_{\text{max}}. \end{aligned} \quad (38)$$

A normalised probability distribution of pericenter distances for encounters in galactic nuclei is plotted in Figure 4a, where we approximated  $\psi_{mM}(r, w)$  as a Maxwellian distribution with variance  $v_c(r)$ . For comparison the distribution function for the Maxwellian core of a star cluster without a central massive BH is plotted in Figure 4b.

### 3.3.3 Eccentricity dependence

We can use Eqs. (21), (22), and (24) to follow the secular evolution of the binary as it passes through the LIGO band and merges when it reaches its last stable orbit. In Figure 5, we have plotted the secular evolution of formed binaries in 10% probability intervals, and plotted the eccentricity after approximately every complete orbit with small circles. Nearly 90% of all binaries actually form within the LIGO band, and  $\approx 94\%$  have an eccentricity  $e > 0.3$  as it enters the LIGO band (when  $f_p = 10 \text{ Hz}$ ). This signature is unique to an active cluster of BHs in a high velocity dispersion environment. For lower velocity dispersions as in star clusters, the

merger distribution of pericenter distances ( $d\Gamma/dr_p$ ) stays uniform out to  $\approx r_{p \max}(2 \times 50 \text{ km s}^{-1}) \approx 260 M_{\text{tot}}$ . In contrast to galactic nuclei, we expect only  $\approx 10\%$  of all binary GW sources in star clusters to have eccentricities higher than 0.3 when they enter the LIGO band, and  $\approx 8\%$  to form within the LIGO band. Binaries which merge due to 3 or 4-body interactions, are even less likely to have such a high eccentricity (Gültekin et al. 2006). O’Leary et al. (2006) calculated the expected distribution of eccentricities for binaries that form in dense star clusters (see their Fig. 3). In their simulations which had over 1000 mergers from random encounters, they had no cases that had an eccentricity  $> 0.3$  when the binary’s GWs entered the LIGO band, and only 3 cases ( $\approx 10^{-3}$ ) with eccentricity  $> 0.1$ . Their calculations also included secular effects which could result in mergers with higher eccentricity (Wen 2003). However, in these cases, the binary must have merged after one Kozai cycle in a hierarchical triple. Since the Kozai cycle is a dynamical effect, it operates on a timescale much shorter than the disruption timescale of the cluster. Thus, any merger due to the Kozai effect would indicate an active cluster of BHs must still exist. This is in contrast to a delayed merger from an ejected binary, which takes of order a Hubble time to merge. We discuss other aspects of GW detection in § 4 below.

In most instances, the first binary forming encounters occur within the LIGO band. However, the S/N of such encounters is too small to be detected for low masses (Kocsis et al. 2006). Therefore, encounters which remain ec-

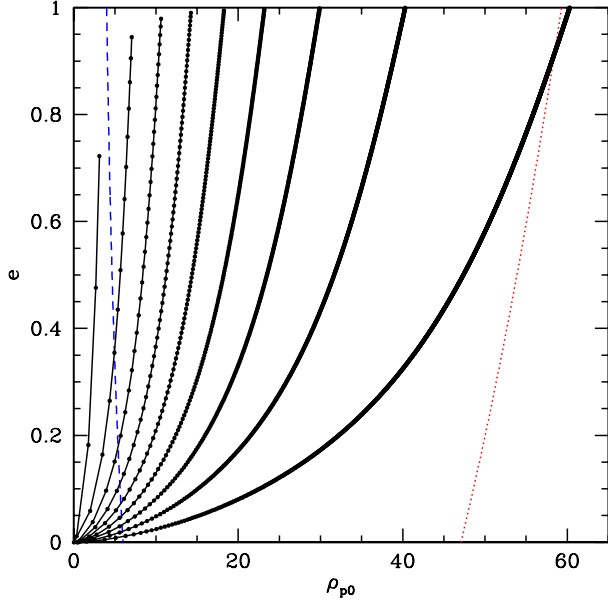


**Figure 5.** The secular evolution of BH binaries. We have plotted in 10% probability intervals the evolution of the binaries as they decay ( $M = m = 10 M_{\odot}$ ; see Fig. 4 for details). The solid line is the orbit averaged evolution given by Eqs. (21) & (22). The solid circles denote the completion of approximately one orbital period,  $\Delta t_{\text{orb}}$ . The gap between the solid line and  $e = 1$  is due to the finite loss of energy during the initial parabolic encounter. For nearly  $\sim 30\%$  of all binaries, the orbit averaged approximation is (visibly) not valid, as can be seen by the large space between each orbit. The dotted (red) line denotes where the binaries peak harmonic is 10 Hz, the lower limit of the LIGO band. Nearly 90% of all binaries that form in galactic nuclei are within this limit upon first passage. The dashed (blue) line denotes the eccentricity at the last stable orbit (Eq. 23).

centric throughout the inspiral, especially near plunge, may be the most readily detectable encounters. Therefore we are interested in the eccentricity of the binary as it reaches the LSO (see Eq. 23). From Eq. (34), and the equation of evolution (Peters 1964, Eq. 24) we solve for the probability distribution of eccentricity at the LSO. We plot the eccentricity distribution at LSO in Figure 6 for both galactic nuclei and globular clusters. For encounters which that to direct plunge, our calculation gives an eccentricity greater than 1. However, for normalisation purposes, we include this in our calculations, as they interestingly comprise a significant fraction of merger events.

Until now, nearly all LIGO sources were expected to have a negligible eccentricity as they enter the LIGO band (but see Mandel et al. 2008, for intermediate mass ratio inspirals in star clusters). The comparatively low eccentricity binary formed through few-body encounters or standard binary evolution circularise before they enter the LIGO band and are detected. Therefore, the detection of eccentric inspirals is a strong test of the formation scenario of nuclear binaries, and can conclusively reveal the origin of the BHs.

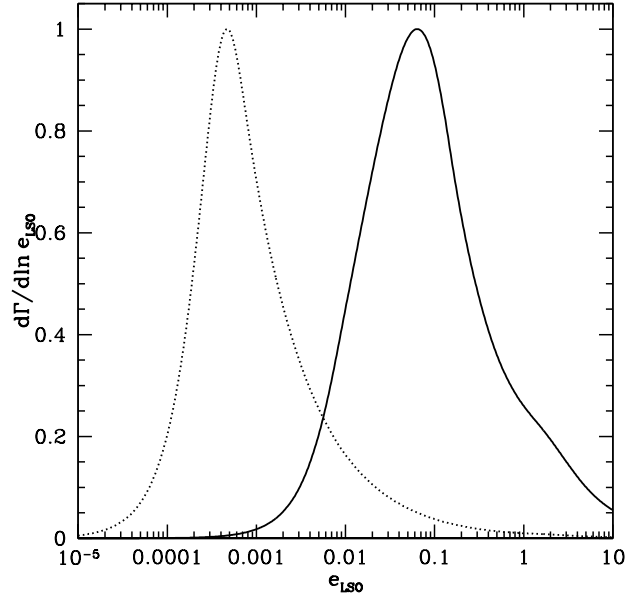


**Figure 6.** The eccentricity distribution of events. Plotted is the eccentricity distribution of mergers at the last stable orbit ( $d\Gamma/d\ln e_{\text{LSO}}$ ) for one example of a galactic nucleus (solid line) and a globular cluster (dotted line). Both lines are normalised so that they reach a maximum value of 1.  $e_{\text{LSO}} \geq 1$  corresponds to encounters that directly undergo a plunge. See the text and Fig. 4 for our assumptions and details of the calculation.

### 3.3.4 Radius Dependence inside the Galactic Nucleus

In Figure 7, we plot the cumulative binary formation rate for radii larger than  $r$ ,  $\Gamma(> r)$ , as well as  $d\Gamma/d\ln r$ . For most models, the total differential rate of binary formation per logarithmic bin is roughly flat. Thus, each logarithmic radius interval contributes equally to the rate. We therefore conclude that the rates determined are rather robust to the depletion of BHs very close to the SMBH as may be caused by resonant relaxation (Rauch & Tremaine 1996; Rauch & Ingalls 1998; Hopman & Alexander 2006a) or our choice of the innermost radius for BHs. In order for the rate to be dominated by mergers at large  $r$ , the number density of the BHs would have to decrease with an exponent  $r^{-\alpha}$  where  $\alpha = p + 3/2 < 3/2$  (see § 2). This is precisely the reason we accounted for the stars in determining the potential in Eq. (6), and did not let the density profile of the BHs and stars go to a constant value as in previous analyses.

We do not expect these tight binaries in their subsequent inspiral phase to have any observable effect dynamically. Overall, we expect  $\sim 10 - 10^3$  such binaries to merge over a Hubble time. This presents a much smaller source of energy than the SMBH, which accretes  $\sim 10^4$  BHs over a Hubble time (FAK06). However small the intrinsic rate in each galaxy, the cumulative merger rate of many galaxies is large enough to be detected by future ground based gravitational wave observatories.

### 3.3.5 Cosmological Merger Rate Density

Using the  $M_{\text{SMBH}} - \sigma_*$  relationship found by Tremaine et al. (2002) for higher mass BHs,

$$M_{\text{SMBH}} \approx 1.3 \times 10^8 M_{\odot} (\sigma_*/200 \text{ km s}^{-1})^4, \quad (39)$$

we can extrapolate our results from § 3.1.1 to a range of galactic nuclei and determine the overall rate of mergers in the Universe. Observations by Barth et al. (2005) & Greene & Ho (2006) have demonstrated that Eq. (39) extends to active SMBHs with masses as low as  $10^5 M_{\odot}$ , well within the range of our interest. We expect the total mass of stars within the radius of influence to be comparable to the mass of the SMBH,  $M(< r_i) \approx 2M_{\text{SMBH}}$ . If these stars follow a radial density profile of  $n_* \propto r^{-3/2}$  as expected for a relaxed system (see § 2), then their number density at the radius of influence is

$$n_*(M_{\text{SMBH}}) \approx 1.2 \times 10^5 \text{ pc}^{-3} \sqrt{10^6 M_{\odot}/M_{\text{SMBH}}}. \quad (40)$$

This gives a number density about 45% larger than assumed in § 2 for the Milky Way and used in our calculations presented in Table 1, but is well within the expected scatter in number densities as we discuss later in this section. The actual number density at the radius of influence for a BH will depend on both the formation history of the galaxy as well as the merger history of the SMBH. Because the merger rate is usually greatest at the smallest radii, we can determine the rate in any nucleus by scaling Eq. (32) and evaluating the integral at  $r_{\text{min}} \propto \sqrt{M_{\text{SMBH}}}$ , the radius where the merger timescale of the BH into the SMBH is approximately a Hubble timescale (approximately the inner radius of BHs). Coincidentally, this radius has the same scaling relation to the outer radius,  $r_{\text{max}} = r_i \propto \sqrt{M_{\text{SMBH}}}$  where we use Eq. (39). The total merger rate,  $\Gamma$  is simply proportional to  $\propto n_{\text{BH}}^2 (b^2 w) r^3$  evaluated at  $r = r_{\text{min}}$ . We can approximate the number density of BHs as  $n_{\text{BH}}(r) \approx C_{\text{BH}} n_*(r_i) (r/r_i)^{-p-3/2}$ . Substituting in  $r_i$ , we get  $n_{\text{BH}}(r_i) \propto M_{\text{SMBH}}^{-1/2}$ , independent of the power-law distribution of BHs,  $p$ . The cross-section of binary capture times the relative velocity is  $\pi b^2 w \propto \omega^{-11/7} \propto M_{\text{SMBH}}^{-11/28}$ , given  $w \propto (M_{\text{SMBH}}/r)^{1/2}$ . Combining these dependencies, we find the merger rate has a relatively weak dependence on the mass of the SMBH,  $\Gamma \propto M_{\text{SMBH}}^{3/28}$ . Over two orders of magnitude in mass, we expect the rate to change only by  $\approx 40 - 60\%$ . To test this scaling relationship we have run a simulation with  $M_{\text{SMBH}} = 10^5 M_{\odot}$  and  $\sigma_* = 30 \text{ km s}^{-1}$ , and found that the rate was in fact comparable to the relationship found here. Any discrepancy is likely due to the slight difference in the capture rate of the BHs and stars (see Eq. [4]).

Although the merger rate of BHs is not very sensitive to the SMBH mass, it is sensitive to the intrinsic scatter of  $n_*$  for each galaxy, which is used to normalise the entire distribution of the BHs (see Eq. [6]). The expected rate of mergers is determined by  $\langle n_*^2 \rangle$ , the average of the number densities squared at the radius of influence for the distribution of galaxies in the universe. Given  $\langle n_*^2 \rangle = \langle n_* \rangle^2 + \sigma_n^2$ , where  $\sigma_n$  is the variance of the number density at the radius of influence of a population of SMBHs, we must rescale our results by a factor

$$\xi = \frac{\langle n_*^2 \rangle}{\langle n_* \rangle^2} = 1 + \frac{\sigma_n^2}{\langle n_* \rangle^2}. \quad (41)$$

Previous studies on GW event rate estimates neglected corrections due to cosmic variance, Eq. (41). However it is quite plausible that *not* all galaxies with the same SMBH mass have exactly the same number of stars in the central cusp. In fact, Merritt et al. (2007) determined the relaxation times for galaxies in the ACS Virgo Survey (Côté et al. 2004), and found a relatively tight correlation, however, there was still significant scatter above the mean by about an order of magnitude. We have taken the results from Merritt et al. (2007) (specifically all nuclei with  $\sigma_* < 140 \text{ km s}^{-1}$  in their Fig. 1), and determined that  $\sigma_n^2 / \langle n_* \rangle^2 \sim 30$ . Although there is considerable uncertainty in the actual value of  $\xi$ , both observationally and theoretically, we expect the merger rate to be larger than we have so far calculated by  $\xi \gtrsim 10-100$ , and scaled our results by  $\xi_{30} = \xi/30$ . In our calculations, however, we use the conservative slope of Eq. (40) to determine the mean value of  $n_*$ , and not the shallower slope found by Merritt et al. (2007), which would give rate estimates to be an order of magnitude larger than found here.

We calculate the average cosmological merger rate density by convolving the rate per galaxy with the number density distribution of SMBHs in the universe. We extrapolate the results of Aller & Richstone (2002), who found the best fit number density distribution of massive SMBHs to be

$$\frac{dn_{\text{SMBH}}}{dM_{\text{SMBH}}} = c_o \left( \frac{M_{\text{SMBH}}}{M_{\bullet}} \right)^{-1.25} e^{-M_{\text{SMBH}}/M_{\bullet}}, \quad (42)$$

assuming this formula is valid all the way to  $M_{\text{SMBH}} = 10^4 M_{\odot}$ , where  $c_o = 3.2 \times 10^{-11} M_{\odot}^{-1} \text{ Mpc}^{-3}$  and  $M_{\bullet} = 1.3 \times 10^8 M_{\odot}$ . Finally, we get the cosmological merger rate by integration,

$$\begin{aligned} \mathcal{R} &= \int_{10^4 M_{\odot}}^{10^7 M_{\odot}} \Gamma_{1\text{GN}}(M_{\text{SMBH}}) \frac{dn_{\text{SMBH}}}{dM_{\text{SMBH}}} dM_{\text{SMBH}} \\ &\approx 3 \Gamma_{1\text{GN}} \xi_{30} \text{ Mpc}^{-3}, \end{aligned} \quad (43)$$

where  $\Gamma_{1\text{GN}}$  is the expected rate of mergers for a single galactic nucleus of a specific model shown in Table 1. The normalisation  $3\xi_{30} \text{ Mpc}^{-3}$  follows from the distribution given in Eq. (42), and also accounts for the intrinsic scatter of  $n_*$  for a population of galaxies, Eq. (41). For our fiducial model of the MW, Model B, we get a comoving rate density of  $8.4 \times 10^{-10} \xi_{30} \text{ yr}^{-1} \text{ Mpc}^{-3}$ . Because this integral is nearly flat in the log of  $M_{\text{SMBH}}$ , it results in a similar rate density per logarithmic mass bin and is not very sensitive to the limits of the integration. Taking the lower limit of currently observed SMBH masses, of  $10^5 M_{\odot}$ , we get a rate  $\approx 60\%$  of what we calculated here. However, recent observations by Greene et al. (2008) have shown that the  $M_{\text{SMBH}} - \sigma$  relation extends to the smallest SMBHs observed, some of which reside in galaxies without a classical bulge. Hence, there is still  $\approx 50\%$  uncertainty in the merger rate due to the true function of  $\Gamma_{1\text{GN}}(M_{\text{SMBH}})$  discussed above, but the total rate density is relatively robust given the other uncertainties in our calculation, especially  $\xi_{30}$  and  $C_{\text{BH}}$ .

For future calculations, we define  $d\mathcal{R}_{mM}/dp_0$  as the rate density for fixed masses  $m$  and  $M$  analogous to Eq. (31) and (34).

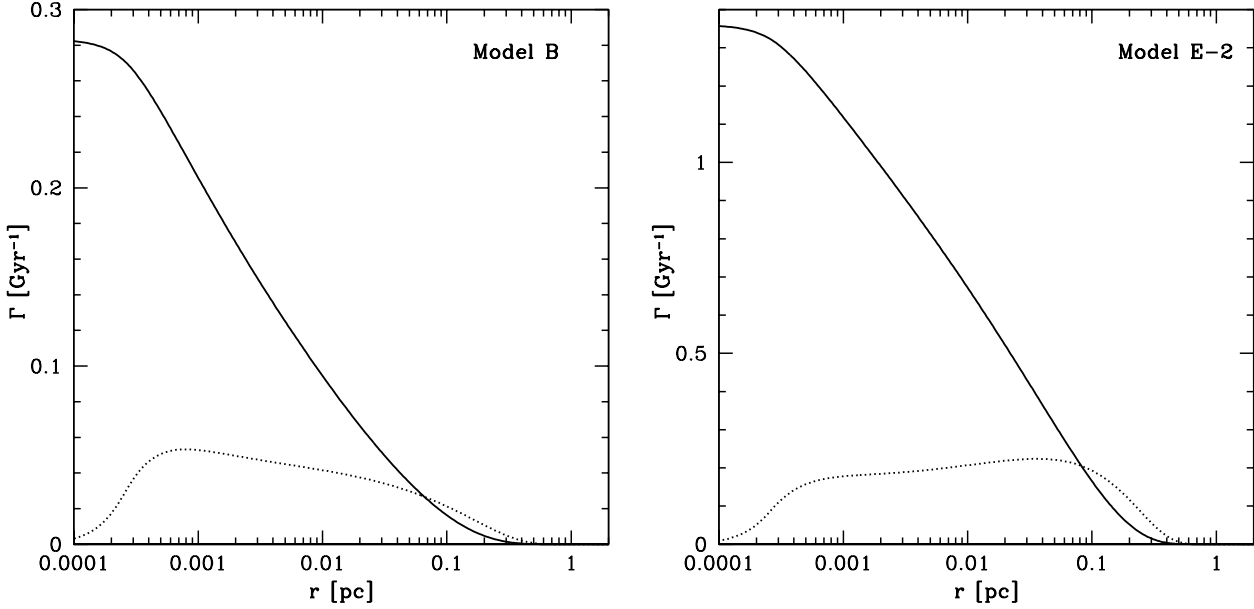


**Figure 7.** Rate of binary formation as a function of the log of the radius for Models B and E-2. The solid line is the cumulative rate of binary formation for radii greater than  $r$ . The dotted line is the differential rate distribution per logarithmic bin ( $d\Gamma/d\log r$ ).

### 3.3.6 Application to Massive Star Clusters

BHs in massive star clusters without a central massive black hole will also undergo an epoch of mass segregation (Kulkarni et al. 1993; Sigurdsson & Hernquist 1993), in which the BHs segregate to the cluster core, and effectively decouple from the stars forming their own subcluster (Portegies Zwart & McMillan 2000; Merritt et al. 2004; O’Leary et al. 2006; Miller & Lauburg 2008). This BH subcluster will continue to interact only with the BHs until a sufficient number of BHs are ejected dynamically, that they come back into equilibrium with the stars. This occurs approximately when  $N_{\text{BH}} \lesssim 100$  (Watters et al. 2000). For massive clusters, with  $\langle w_{\text{BH}} \rangle \approx 15 \text{ km s}^{-1}$  and  $n_{\text{BH}} \sim 10^6 \text{ pc}^{-3}$ , the cluster evaporates before about  $\lesssim 10^8 - 10^9 \text{ yr}$ . Scaling Eq. (32) to these parameters, the cluster will have a BH-BH merger rate of

$$\begin{aligned} \Gamma_{\text{IMSC}} &\approx N_{\text{BH}} \langle n_{\text{BH}} w_{\text{BH}} \sigma_{cs} \rangle \\ &\approx 1.8 \times 10^{-8} \text{ yr}^{-1} \times \left( \frac{N_{\text{BH}}}{1000} \right) \left( \frac{n_{\text{BH}}}{10^6 \text{ pc}^{-3}} \right) \\ &\quad \times \left( \frac{w_{\text{BH}}}{15 \text{ km s}^{-1}} \right)^{-11/7}, \end{aligned} \quad (44)$$

during this period of evolution, if the number density of BHs is uniform in radius. This is comparable to, but slightly less than merger the rate found by O’Leary et al. (2006) for the early evolution of a cluster of BHs due to three-body and four-body encounters alone. The detection rate of such early mergers depends on the number of *young* clusters (with  $t_{\text{age}} \lesssim 10^8 - 10^9 \text{ yr}$ ) within the detection limit of LIGO. Globular clusters, an important source of delayed mergers, are too old to still have a BH subcluster. However, the young clusters in star burst galaxies would be an excellent source if they survive sufficiently long in their hosts to undergo this process of mass segregation (O’Leary et al. 2007).

The eccentricity distribution of binary capture mergers in star clusters is plotted in Figure 6. Overall, the rate of mergers in star clusters is dominated by small eccentricity events, which would be detected as circular inspirals by ground-based gravitational wave detectors. However, young star clusters may have as many, or even more, eccentric mergers than are expected in the nuclei of galaxies if there are a sufficient number of mergers in young star clusters. In massive star clusters, we expect  $\sim 10\%$  of all gravitational wave captures to merge with eccentricities similar to those in galactic nuclei. Therefore, the distribution of low eccentricity events will be indicative of the source of BH-BH mergers, and may be useful in constraining the distribution and evolution of BHs in both galactic nuclei and massive star clusters.

## 4 DETECTION OF GRAVITATIONAL WAVES

To determine the expected detection rate of sources, we must now calculate the maximum luminosity distance to which these inspirals are detectable. In this section, we discuss the general properties of the waveform, calculate the maximum distance of detection, and add up the total expected detection rate for second generation terrestrial GW instruments.

### 4.1 General Properties of the Inspiral

The evolution of the binary and the GW signal can be separated into three phases:

- [I] Highly eccentric encounters – train of distinct GW bursts in time, broadband signal in frequency.
- [II] Moderate-small eccentricity inspiral – continuous GW signal in time, dominated by distinct frequency harmonics.
- [III] Merger and ringdown – short duration peak GW power and exponential decay.

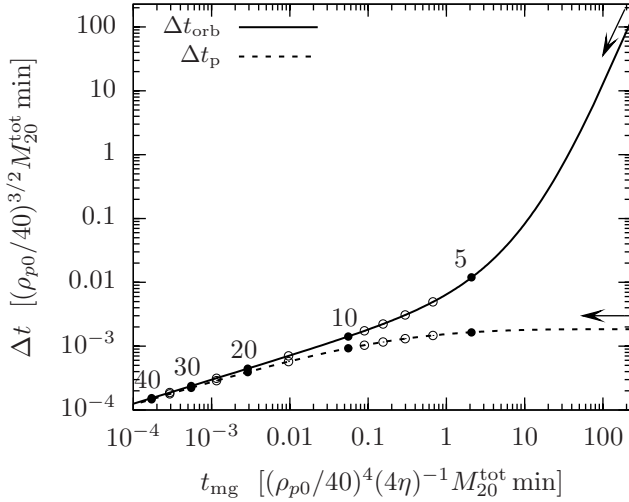


**Figure 8.** The relevant timescales that determine the GW waveform: the evolution of the orbital time ( $\Delta t_{\text{orb}}$ ) and the time duration of pericenter passage ( $\Delta t_p$ ) as functions of time to merger ( $t_{\text{merger}}$ ). The units are minutes on both axes for  $(M, \eta, \rho_{p0}) = (20, .25, 40)$  and are different for other values as marked. Similar to Fig. 3 the orbits should not be extrapolated beyond the LSO for a particular  $\rho_{p0}$ , shown with circles. The inspiral is quasiperiodic if  $\Delta t_{\text{orb}} \ll t_{\text{merger}}$  and  $\Delta t_p \ll t_{\text{merger}}$ . The GW signal is burstlike if  $\Delta t_p \ll \Delta t_{\text{orb}}$  and is continuous if  $\Delta t_p \sim \Delta t_{\text{orb}}$ .

The distinction between Phases **I** and **II** can be understood by studying the evolution of the relevant timescales that determine the GW waveform: the orbital time ( $\Delta t_{\text{orb}} = \omega_{\text{orb}}^{-1}$ ), and the time duration of pericenter passage ( $\Delta t_p = \omega_p^{-1}$ ). These are plotted in Figure 8 as a function of time to merger  $t_{\text{mg}}$ . For both Phases **I** and **II**,  $|\text{d}\Delta t_{\text{orb}}/\text{d}t_{\text{mg}}| \ll 1$ , so the orbit is quasiperiodic and evolves gradually due to the emission of GWs. The characteristic GW emission timescale during each orbit is determined by  $\Delta t_p$ . Figure 8 shows that initially (Phase **I**),  $\Delta t_p \ll \Delta t_{\text{orb}}$ , implying that the waveform consists of a train of short  $\Delta t_p$  duration bursts arriving quasiperiodically with separation  $\Delta t_{\text{orb}}$ . Later, when the burst duration timescale  $\Delta t_p$  becomes comparable to  $\Delta t_{\text{orb}}$ , the signal becomes continuous in time domain (Phase **II**). Since the orbital evolution is quasiperiodic, the GW signal is approximately a sum of discrete frequency harmonics of the orbital frequency,  $f_{\text{orb}}$ . When the eccentricity becomes relatively small  $e \lesssim 0.7$ , (Phase **II**) the harmonic decomposition is quickly convergent, while during Phase **I**, it is more convenient to work with the continuous limit of the frequency spectrum.

During Phase **I** and **II** the equations of motion and the GW waveforms can be calculated accurately in various approximations (see § 1.1 above). For Phase **II**, the expected signal to noise ratio of detection has been calculated by Barack & Cutler (2004), and the  $e = 1$  parabolic case was examined in Kocsis et al. (2006). In the following, we generalise these studies to be applicable to Phases **I** and **II**.

Once the orbital separation reaches the last stable orbit, the BHs fall in rapidly and form a common horizon. The last stable orbit, which marks the end of Phase **II**, is determined by the initial pericenter distance  $\rho_{p0}$  for an initially parabolic orbit shown by circles in Figure 8. The GW waveform during Phase **III** involves the calculation of the violently chang-

ing spacetime and the eventual relaxation into a Kerr BH. This requires full numerical simulations of the Einstein equations. The detectability of the resulting waveforms have been examined for nonspinning binaries and quasircular initial conditions (Baker et al. 2007; Berti et al. 2007). These studies have shown that  $S/N = 10$  can be reached up to a distance  $d_L = 1 - 6$  Gpc for total binary mass  $M_{\text{tot}} = 10 - 200 M_{\odot}$  for AdLIGO. Eccentric mergers were considered very recently by Hinder et al. (2008a,b) and Washik et al. (2008) for the case of no initial spins, who showed that the resulting GW power is comparable to (or sometimes larger than) the power released during quasircular mergers. Future studies should address spin effects during the coalescence, they might significantly modify the GW power and waveforms.

We note that the separation between Phases **I-II-III** is valid only if the initial encounter has a minimum separation,  $r_{\text{UCO}} \sim 2 - 4 M_{\text{tot}}$ , depending on BH spins. Direct captures, or orbits outside but repeatedly approaching the unstable circular orbit (the so-called ‘zoom-whirl’ orbits), are qualitatively different. Such encounters have been studied in the geodesic approximation appropriate for extreme mass ratios (Gair et al. 2005, 2006; Pretorius & Khurana 2007; Levin & Perez-Giz 2008) and using full numerical simulation for equal masses (Hinder et al. 2008a). In this case the GW spectrum is considerably different and the power is considerably increased.

The purpose of this section is to derive the signal-to-noise ratio for the quasiperiodic Phases **I** and **II** and determine the maximum range of detection for second generation terrestrial GW instruments. We leave the assessment of Phase **III** and the zoom-whirl domain to future studies.

## 4.2 Signal to Noise Ratio

Here we briefly review the general calculation of the signal to noise ratio for detecting the GW signal, which we can then utilise for the waveforms generated by GW capture events. We refer the reader to Flanagan & Hughes (1998) for more details.

In general, the signal to noise ratio of a GW detection is defined as

$$\frac{S^2}{N^2} = 4 \int_{f_{\text{min}}}^{f_{\text{max}}} \frac{|h^2(f, \boldsymbol{\theta})|}{S_h(f)} \text{d}f, \quad (45)$$

where  $h(f, \boldsymbol{\theta})$  is the Fourier transform of the GW signal weighted by the antenna beam patterns,  $\boldsymbol{\theta} = \{\theta_i\}$  are the physical parameters describing the source and the detector orientation,  $S_h(f)$  is the one-sided noise spectral density in units of  $\text{Hz}^{-1}$ , and  $f_{\text{min}} \leq f \leq f_{\text{max}}$  correspond to the frequency band of the instrument, e.g.  $(f_{\text{min}}, f_{\text{max}}) \approx (10, 10^4)$  Hz for AdLIGO<sup>5</sup>.

The sky position and binary orientation averaged root mean square signal-to-noise for a single orthogonal arm interferometric GW instrument is

$$\left\langle \frac{S^2}{N^2} \right\rangle = \int_{f_{\text{min}}}^{f_{\text{max}}} \frac{h_c^2(f)}{5f S_h(f)} \frac{\text{d}f}{f}, \quad (46)$$

<sup>5</sup> <http://www.ligo.caltech.edu/advLIGO/scripts/summary.shtml>

where  $h_c(f)$  is the characteristic isotropic GW amplitude defined as

$$h_c = \frac{1}{\pi d_L} \sqrt{2 \frac{dE}{df}} = \frac{1}{\pi d_L} \sqrt{\frac{2\dot{E}}{f}}, \quad (47)$$

where  $d_L(z)$  is the luminosity distance to a source at a cosmological redshift  $z$ ,  $dE/df$  is the one-sided GW energy spectral density on a spherical shell at infinity. The second equality corresponds to the stationary phase approximation for a quasiperiodic signal sharply peaked at frequency  $f$ . In this case,  $\dot{E}$  is the total GW power at frequency  $f$ , which evolves slowly in time according to its time derivative  $\dot{f}$ .

Equations (46) and (47) can be generalised for a signal consisting of discrete harmonics  $f_n$ , with negligible overlap as (Barack & Cutler 2004)

$$\left\langle \frac{S^2}{N^2} \right\rangle = \sum_{n=2}^{\infty} \int_{f_{\min}}^{f_{\max}} \frac{h_{c,n}^2(f_n)}{5f_n S_h(f_n)} \frac{df_n}{f_n}, \quad (48)$$

and

$$h_{c,n} = \frac{1}{\pi d_L} \sqrt{\frac{2\dot{E}_n}{f_n}}, \quad (49)$$

where  $\dot{E}_n$  is the GW power radiated at frequency  $f_n$ . For quasiperiodic orbits with an intrinsic orbital frequency  $f_{\text{orb}}$ , the observed frequency harmonics at redshift  $z$  are given by

$$f_n \equiv n f_{\text{orb},z} \equiv n \frac{f_{\text{orb}}}{1+z}. \quad (50)$$

### 4.3 Application to the GW Capture Process

Let us now turn to the detectability of the GWs starting from the initial hyperbolic encounter and ending in the violent BH merger. Here we derive a computationally more efficient equivalent form of Eq. (48), which can be utilised for Phases **I** and **II**.

Following Barack & Cutler (2004), we calculate the binary evolution and the GW signal waveform in the leading order approximation of Peters & Mathews (1963), where the interacting masses move on quasi-Newtonian trajectories and emit quadrupolar radiation. This approximation is adequate in terms of the angular-averaged  $S/N$  if the initial periaapse is well outside the unstable circular orbit, e.g.  $r_p \gg r_{\text{UCO}}$ . At smaller initial  $r_p$ , the Newtonian approximation underestimates the GW power and is therefore conservative.<sup>6</sup> To lowest order,

$$\dot{E}_n = \frac{32}{5} \eta^2 M_{\text{tot}}^{10/3} \omega_{\text{orb}}^{10/3} g(n, e), \quad (51)$$

where  $g(n, e)$  determines the relative power of the  $n$ th harmonic for orbits with eccentricity  $e$ , which is given by Peters & Mathews (1963) in the Newtonian approximation

as

$$g(n, e) = \frac{n^4}{32} \left\{ \left[ J_{n-2} - 2eJ_{n-1} + \frac{2}{n}J_n + 2eJ_{n+1} - J_{n+2} \right]^2 + (1-e^2)[J_{n-2} - 2J_n + J_{n+2}]^2 + \frac{4}{3n^2}J_n^2 \right\}. \quad (52)$$

Here  $J_i(x)$  is the  $i$ th Bessel function, and we have suppressed the argument  $x = ne$ , i.e.  $J_i \equiv J_i(ne)$  for each  $i$  above. These waveforms generally have a maximum at frequency  $\omega_p$  for  $e \gtrsim 0.5$  and have a steep cutoff such that the fractional GW power beyond  $5\omega_p$  is smaller than  $10^{-3}$  (Turner 1977). For smaller  $e$ , the harmonics beyond the first  $2\omega_p$  are greatly suppressed. The number of harmonics necessary to a precision  $10^{-3}$  can be estimated as

$$n_{\max} = 5 \frac{\omega_p}{\omega_{\text{orb}}} = 5 \frac{(1+e)^{1/2}}{(1-e)^{3/2}} \quad (53)$$

e.g.  $n_{\max} = (10, 40, 10^4)$  for  $e = (0.3, 0.7, 0.99)$ , respectively.

Note that Eq. (51) depends explicitly on  $e$ . Therefore in order to directly evaluate the  $S/N$  integral in Eq. (48) over  $f_n$  one needs to invert the frequency evolution equation  $f_n(r_{p0}, e_0, e)$ . Computationally it is much more efficient to change the integration variable from  $f_n$  to  $e$ ,

$$\frac{df_n}{f_n} = -\frac{3}{2} d \ln \frac{a}{a_0} = -\frac{18}{19} \frac{1 + \frac{73}{24}e^2 + \frac{37}{96}e^4}{1 - \frac{183}{304}e^2 - \frac{121}{304}e^4} \frac{de}{e}, \quad (54)$$

and reverse the order of the sum and the integral

$$\left\langle \frac{S^2}{N^2} \right\rangle = \frac{48}{95} \frac{\eta M_{\text{tot},z}^3 \rho_{p0}^2}{d_L^2} \int_{e_{\text{LSO}}}^{e_0} \sum_{n=2}^{n_{\max}(e)} \frac{g(n, e) s(e, e_0)}{n^2 S_h(f_n)} \frac{de}{e}, \quad (55)$$

where  $e_{\text{LSO}}$  corresponds to the particular  $\rho_{p0}$  (see Eq. 23),  $e_0$  is given by Eq. (16), and

$$s(e, e_0) = \left( \frac{e}{e_0} \right)^{\frac{24}{19}} \left( \frac{1 + \frac{121}{304}e^2}{1 + \frac{121}{304}e_0^2} \right)^{\frac{1740}{2299}} \frac{(1 + e_0^2)(1 - e^2)^{3/2}}{1 - \frac{183}{304}e^2 - \frac{121}{304}e^4}. \quad (56)$$

Note, that  $S_h(f) = \infty$  is assumed outside of  $f_{\min} \leq f \leq f_{\max}$ . The upper limit of the sum in this form can be adjusted to the required calculation precision using Eq. (53).

For Phase **II**, we can rewrite Eq. (55) by changing the sum over  $n$  to a continuous integral over  $f_n$ .

$$\left\langle \frac{S^2}{N^2} \right\rangle = \frac{48}{95} \frac{\eta M_{\text{tot},z}^3 \rho_{p0}^2}{d_L^2} \int_{e_{\text{LSO}}}^{e_0} \int_{f_{\min}}^{f_{\max}} \frac{g(n, e) s(e, e_0)}{f_{\text{orb},z} S_h(f)} \frac{df de}{f e}. \quad (57)$$

where  $n = f/f_{\text{orb},z}$ ,  $f_{\text{orb},z} = f_{\text{orb}}(r_{p,z}, e, e_0)$  given above by Eq. (50), and  $r_{p,z} = M_{\text{tot},z} \rho_{p0} = (1+z)M_{\text{tot}} \rho_{p0}$ .

In addition to their numerical advantages, Eqs. (55) and (57) can be used to study the time-frequency evolution of the instantaneous  $S/N$  accumulation rate as the orbit evolves. Figure 9 shows the contribution of the first  $n \leq 100$  harmonics to the signal-to-noise ratio for AdLIGO (i.e. before evaluating the sum or the integral in Eq. 55) for total masses  $M_{\text{tot}} = (20, 60)M_{\odot}$  and initial periaapse  $\rho_{p0} = (10, 20, 40)$ . The figure illustrates the unique frequency evolution of the signal consistent with the expectations described above. Initially during Phase **I**, it is broadband in frequency, and decouples into discrete harmonics at smaller eccentricities during Phase **I**. The contribution of upper harmonics is nonnegligible even at LSO, especially if the initial periaapse satisfies

<sup>6</sup> Modulations due to general relativistic pericenter precession and relativistic beaming would be very important for the real data analysis, but not in terms of the the calculation of event rates that depend on the angular-averaged total  $S/N$ .

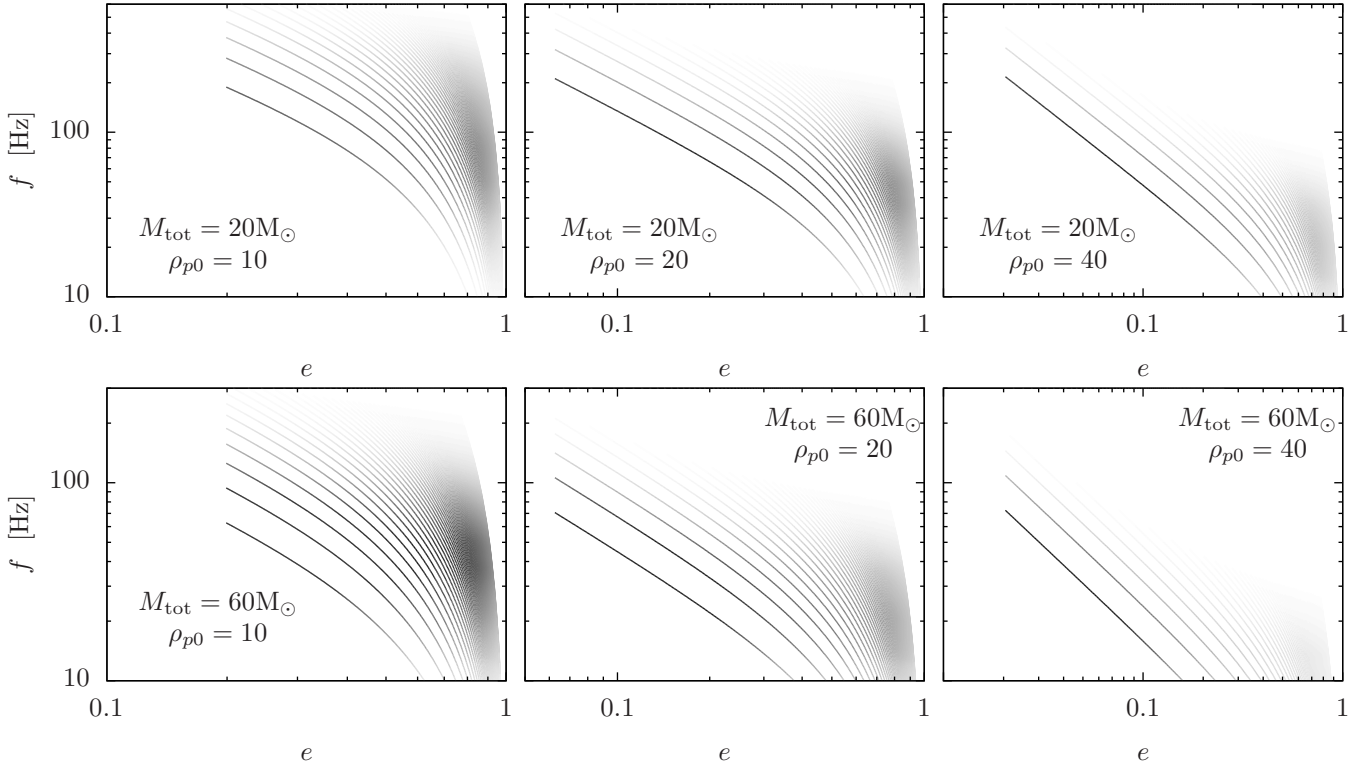


**Figure 9.** The frequency evolution of GWs as a function of eccentricity for various total mass and initial periapsis as labelled. The shading represents the expected signal-to-noise ratio of the first  $n = 100$  harmonics per logarithmic eccentricity bins for AdLIGO. The waveform is described by a broadband spectrum at large  $e$  (Repeated Burst Phase) that later separates into distinct harmonics as eccentricity decreases until the LSO (Eccentric Inspiral Phase). The signal-to-noise ratio is substantial already at  $e \gtrsim 0.7$ .

$\rho_{p0} \lesssim 40$ . Note that the maximum frequency of the  $S/N$  at large eccentricities  $e \gtrsim 0.8$  in Figure 9 is merely a consequence of not plotting harmonics beyond  $n = 100$ , leading to a large underestimate of  $S/N$  in Phase II. In this case Eq. (57) becomes more useful than Eq. (55).

The frequency-independent  $S/N$  accumulation rate can be obtained as a function of eccentricity (or time using the  $e(t)$  dependence shown in Fig. 3), if evaluating the sum over  $n$  in Eq. (55) or the integral over  $df/f$  in Eq. (57), but not the integral over eccentricity. Figure 10 shows the result for the same masses and periapsis as Fig. 9, including an additional extreme case of  $M_{\text{tot}} = 700M_{\odot}$ . For BH masses below  $M_{\text{tot}} \sim 100$ , the  $S/N$  contribution of the high and low eccentricity phases are comparable. The  $S/N$  during highly eccentric encounters dominate for the typical case  $M_{\text{tot}} \sim 20M_{\odot}$  for  $\rho_{p0} \lesssim 20$ , while small  $e$  dominates for larger masses  $M_{\text{tot}} \sim 60M_{\odot}$  for  $\rho_{p0} \gtrsim 20$ . It is very interesting that the eccentric encounters between binaries with intermediate masses up to  $M_{\text{tot}} = 700M_{\odot}$  are detectable to  $\approx 1$  Gpc for close encounters  $\rho_{p0} \lesssim 10$  with AdLIGO, because these masses are otherwise totally invisible during a circular inspiral. This is explained by the broadband nature of the signal during Phase I, leading to nonnegligible power leaking into the detectable frequency range of the detector  $f \gtrsim 10$  Hz. Such massive BHs were thought to be accessible only during the violent merger/ringdown phase for AdLIGO (Flanagan & Hughes 1998; Baker et al. 2007).

The total  $S/N$  can be obtained by evaluating both the sum and the integrals in Eqs. (55) and (57). The result can

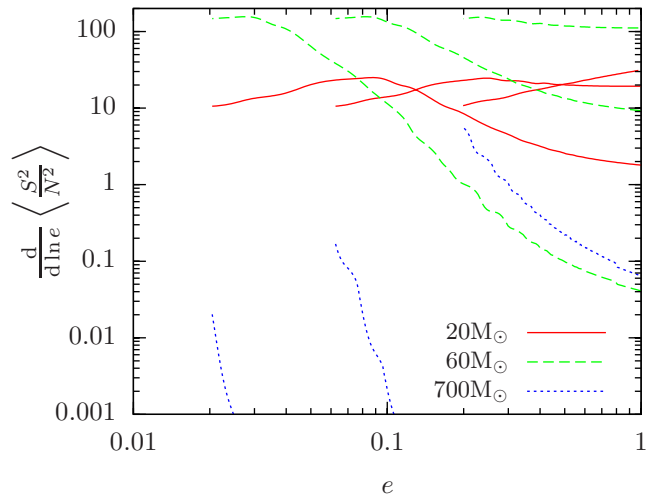


**Figure 10.** The square of the signal-to-noise ratio per logarithmic eccentricity bin as a function of eccentricity for AdLIGO at 1 Gpc. Three sets of curves are shown for total masses with different line types as labelled and initial periapsis  $\rho_{p0} = (10, 20, 40)$  from right to left corresponding to Figure 9. Eccentric encounters between massive black holes are detectable up to  $700M_{\odot}$  with AdLIGO that are totally invisible during a circular inspiral.

be converted into a maximum distance of detection assuming

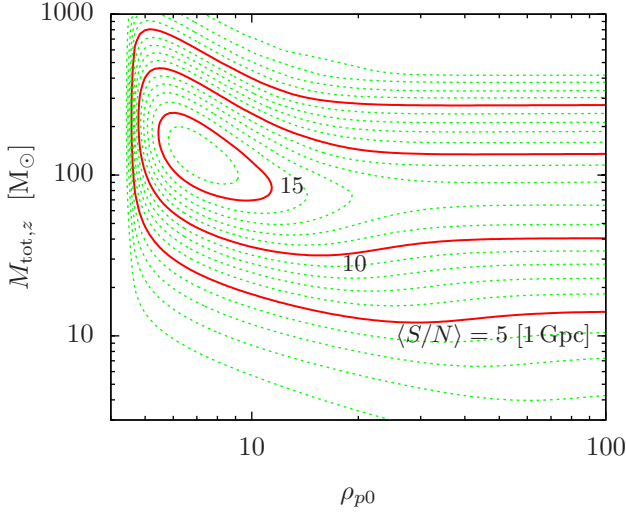


**Figure 11.** The total signal-to-noise ratio contours as a function of the pericenter separation  $\rho_{p0}$  of the first passage and total binary mass,  $M_{\text{tot},z}$  for AdLIGO for an equal-mass binary at 1 Gpc. Different contours show  $\langle S^2/N^2 \rangle^{1/2}$  (averaged over the binary orientation and sky position) increasing in steps of 5 for the solid and 1 for the dotted lines. For other mass ratios the SNR is reduced by  $(4\eta)^{1/2}$ . The limit  $\rho_{p0} \rightarrow \infty$  corresponds to circular inspirals in the AdLIGO band, which result in typically a smaller  $S/N$  than most likely events with  $\rho_{p0} \lesssim 40$ . Note that different solid contours correspond to a maximum distance of detection increasing in steps of Gpc for a detection threshold  $S/N = 5$ .

a detection threshold, e.g.  $\langle S^2/N^2 \rangle \equiv 5^2$ . For Phase II,

$$d_L^{\text{max}} = \sqrt{\frac{48 \eta M_{\text{tot},z}^3 \rho_{p0}^2}{95 \langle S^2/N^2 \rangle} \int_{e_{\text{LSO}}}^{e_0} \sum_{n=2}^{n_{\text{max}}(e)} \frac{g(n, e) s(e, e_0)}{n^2 S_h(f_n)} \frac{de}{e}}, \quad (58)$$

and similarly for Phase I. Note, that the integral depends on two parameters  $M_{\text{tot}}$  and  $\rho_{p0}$  and is independent of the mass ratio  $\eta$ .

Figure (11) shows contours of  $d_L^{\text{max}}$  for masses  $2M_{\odot} \leq M_{\text{tot}} \leq 1000M_{\odot}$  and initial periastron  $4 \leq \rho_{p0} \leq 100$ . For the limit of large  $\rho_{p0}$ , the signal is circularised when it arrives in the LIGO band, corresponding to the circular inspiral. The figure shows that the eccentric inspirals can be detected just to a slightly larger distance than the circular inspirals for masses  $M_{\text{tot}} \leq 20M_{\odot}$ . The difference becomes more pronounced at much larger masses. A  $100M_{\odot}$ – $100M_{\odot}$  eccentric inspiral is detectable up to  $3\times$  farther than a standard  $10M_{\odot}$ – $10M_{\odot}$  circular inspiral. For even larger masses,  $d_L^{\text{max}}$  decreases, but remains nonnegligible up to  $M_{\text{tot}} = 700M_{\odot}$ . Currently less is known about the existence of such intermediate mass black holes in galactic cusps, which makes it very difficult to make any theoretical estimates on the expected rates of such encounters. It is possible that AdLIGO will provide the first direct observational limit on the population of these objects. We explore this along with other estimates of the detection rate in § 4.4.

#### 4.4 Detection Rate Estimates

We set  $\langle S^2/N^2 \rangle^{1/2} \geq 5$  as our detection threshold for a single GW instrument, and determine the volume averaged

maximum luminosity distance for detection for each pair of masses,  $d_L^{\text{max}}(m, M)$  from Eq. (58), assuming a uniform distribution of  $r_p$  out to  $r_{p\text{max}}$ . Thus, the total detection rate for Advanced LIGO is estimated to be

$$R = \int_0^{\rho_{p0}^{\text{max}}} d\rho_{p0} \int_{M_{\text{min}}}^{M_{\text{max}}} \int_M^{M_{\text{max}}} dm dM \int_0^{z_{\text{max}}} dz \frac{dV_{\text{co}}}{dz} \times \frac{1}{1+z} \frac{\partial^3 \mathcal{R}}{\partial \rho_{p0} \partial m \partial M} \quad (59)$$

where  $\partial^3 \mathcal{R} / \partial \rho_{p0} \partial m \partial M$  is the comoving partial binary formation rate density between masses  $(m, M)$  at initial periastron  $\rho_{p0}$ , given by Eqs. (31) and (43), averaged over the distribution of  $M_{\text{SMBH}}$  and the number density normalisation  $n_*$  (see Eq. 42 and 43) at redshift  $z$ ,  $n_{\text{gal}}$  is the comoving number density of galaxies at redshift  $z$ ,  $z_{\text{max}}$  is the maximum detectable distance corresponding to  $d_L^{\text{max}}(\rho_{p0}, m, M)$ , and  $dV_{\text{co}}/dz$  is the comoving volume density corresponding to the given cosmology. In practice, however, we calculate  $R$  discretely and ignore cosmological effects, which are not relevant for the next generation of GW instruments,

$$R \approx \sum_{M, m < M} \int_0^{\rho_{p0}^{\text{max}}} d\rho_{p0} \frac{d\mathcal{R}_{mM}}{d\rho_{p0}} \frac{4\pi}{3} (d_L^{\text{max}})^3, \quad (60)$$

where  $d\mathcal{R}_{mM}/d\rho_{p0}$  is the differential rate density of binary formation between mass bins  $m$  and  $M$  (see Eqs. 31 and 43). The resulting total detection rates are shown in the last column of Table 1. Note that the dependence of  $d_L^{\text{max}}$  on the binary parameters  $(\rho_{p0}, m, M)$  lead to an observational bias. For example, since  $d_L^{\text{max}}$  is relatively larger for  $\rho_{p0} \sim 10$ , the detection rate of these encounters is enhanced relative to larger and smaller  $\rho_{p0}$ , even though the intrinsic rate of these encounters is independent of  $\rho_{p0}$ . We have plotted the differential detection rate as a function of  $\rho_{p0}$  in Figure 12 for all mergers as well as each mass bin.

Overall, the most massive BHs in galactic nuclei dominate the detection rate of mergers for AdLIGO. In Figure 13, we have plotted the distribution of detectable mergers as a function of radius for the entire population of BHs, as well as for each mass bin. The clear domination of the high mass BHs is caused by a combination of three important factors: (i) their number density is significantly enhanced by mass segregation (§ 2); (ii) the signal of the event is much stronger for larger masses (e.g., Eqs. 55 & 57); and (iii) the cross-section for binary capture is greater for larger masses (e.g., Eq. 17).

As discussed in § 4.3, we expect the actual inspiral of a BH with an IMBH may be revealed by AdLIGO if the event is sufficiently eccentric during plunge. Although we cannot properly account for this in our analysis, we can attempt to compare the rate to what we have done in this work. For a large mass ratio,  $m \gg M$ , the overall cross-section for forming binaries increases roughly as  $b^2 \propto m^{12/7}$ . Compared to  $10M_{\odot}$  BHs, we expect a  $1000M_{\odot}$  BH to have a gravitational wave capture event  $\sim 3000$  times as often as a single BH. However, the number of IMBHs in the region is very uncertain. If we take the optimistic number of  $\sim 10$  IMBHs in a single galactic nucleus as a steady state distribution (Portegies Zwart et al. 2006), then we expect a comparable total number of events to  $10M_{\odot}$ – $10M_{\odot}$  BH-BH inspirals.

Our analysis in § 2 suffers from inaccuracies for the most massive and rarest BHs. Equation 2 was derived assuming a constant density core (and constant relaxation timescale) for large  $r$  (BW76), which is clearly violated in most galactic nuclei. Typically, the total number of BHs in galactic nuclei decreased with  $M_{\max}$ . Despite this decrease in number, we likely cannot extrapolate our calculations to higher mass BHs such as IMBHs, in order to see what effect they have on flattening the density profile of stellar mass BHs.

## 5 SUMMARY AND DISCUSSION

In this paper, we have analysed two separate problems. First we determined the multi-mass distribution of BHs in galactic nuclei, which we then used to analyse the detection rate and merger of gravitational wave capture binaries. We integrated the time-dependent Fokker-Planck equations for a variety of BH mass distributions until they reached a steady state. We found, consistent with previous results, that within a relaxation timescale at the radius of influence of the SMBH, the BHs and stars form approximately power-law density cusps ( $\propto r^{-3/2-p_0 m/M_{\max}}$ ) within the radius of influence of the SMBH. Because the BHs are more massive than the stars, they have steeper density profiles ( $\propto r^{-2}$ ) and dominate the dynamics and relaxation processes in the inner  $\sim 0.1$  pc near the SMBH.

In such dense population environments, the probability of close flybys between two BHs is nonnegligible. Using our results for the steady-state distribution of BHs, we calculated the expected rate and distribution of GW capture binaries in galactic nuclei. We showed that after forming, these binaries rapidly inspiral and merge within hours. Unlike other sources of merging binaries, the BH binaries in galactic nuclei form with a characteristic GW frequency *inside* the AdLIGO frequency band, and the detectable GW signal duration is much longer compared to circular inspirals. In addition, for sufficiently small impact parameters, the waveforms for such eccentric inspirals are broadband, and can be detected for much larger masses, up to  $M_{\text{tot}} \gtrsim 700 M_{\odot}$ . This exceeds the BH masses previously considered detectable (Brown et al. 2007; Mandel et al. 2008), and as such it opens a new avenue to probe for the existence of a population of intermediate mass black holes in galactic nuclei.

Additionally in § 3.3.6, we also estimated the rate of GW captures in young, massive star clusters where BHs decouple from stars to form a subcluster in the centre. We found that the rate of GW captures in a single cluster may be intrinsically larger than in a galactic nucleus. Typically, most binaries circularise before becoming detectable, however a significant fraction ( $\sim 10\%$ ) may still merge with residual eccentricity. Given the vastly different eccentricity distribution of mergers in galactic nuclei and massive star clusters, the dominate source of eccentric inspirals can be determined with only a few detections. The total rate of such events from massive clusters depends on the relatively unconstrained number of young clusters within the detection limits of AdLIGO.

Finally, we analysed the properties of the GW signal for the eccentric inspiral of comparable mass BHs, starting from the initial highly eccentric phase up to the fi-

nal eccentric inspiral. We found that the maximum luminosity distance that such events may be detected using a single AdLIGO-type interferometer is 1.2 Gpc for component masses  $m = M \sim 10 M_{\odot}$ , and up to 3.3 Gpc for  $m = M \sim 50 M_{\odot}$ . We then used this to calculate the total detection rate of signals, by using a model merger rate convolved with a realistic population of SMBHs. We found that the most massive BHs dominate the detection rate of future ground based gravitational wave detectors with  $\sim (10 - 10^3)\xi_{30}$  events expected per year, where  $\xi_{30}$  is a measure of the expectation value for the square of number densities near the SMBH (see Eq. 41). The overall detection rate is sensitive to the number fraction of BHs as well as the maximum mass of BHs, and so future observations will be able to constrain both the average star formation properties and upper mass of BHs in galactic nuclei.

Overall, the expected AdLIGO detection rate for GW capture binaries in galactic nuclei is comparable to estimates for other sources of gravitational waves. BH-BH binaries that form dynamically in massive star clusters may be detected by AdLIGO  $\sim 10 - 10^4$  times per year, depending on the total fraction of star formation that occurs in massive, long lived clusters (Portegies Zwart & McMillan 2000; Gültekin et al. 2004; O’Leary et al. 2006; Gültekin et al. 2006; O’Leary et al. 2007; Miller & Lauburg 2008). Estimates for the population of merging binaries that formed in the early evolution of present day globular clusters are  $\sim 10 - 100 \text{ yr}^{-1}$  alone. Although globular clusters contain only a small fraction of the mass of stars in the universe, the merger rate of BHs is sufficiently enhanced by dynamical interactions that the rate is comparable to those expected from standard binary evolution for all other stars (Belczynski et al. 2002, 2004; Sadowski et al. 2008; however see Belczynski et al. 2007). Merging neutron stars are also a promising source of gravitational waves, whose progenitors have been directly observed. Using constraints from the modest population neutron star-neutron star binaries known in our galaxy, Kalogera et al. (2004a,b) estimate that  $\sim 20 - 600$  events per year may be detected by AdLIGO. We emphasise that the rates of GW captures calculated in this paper are *independent* of other sources of GWs, and will occur in addition to other sources. Given the estimates of sources from a variety of environments, gravitational wave detectors promise to open a new and interesting window into the physics, dynamics, and evolution of compact binaries.

So far, we have not looked at the interaction between the BHs and other compact objects such as neutron stars (NSs). The NSs are not expected to segregate significantly in galactic nuclei, however they are intrinsically more common than BHs. To test their importance we have performed an additional run of Model E-2 to look at the expected detection rate of NS-BH mergers. We found that the total detection rate of such events is about  $\sim 1\%$  of the total rate ( $\sim 1 \text{ yr}^{-1}$ ), and merits future study. Gravitational waves from BH-NS inspirals can provide interesting constraints on the equation of state for NSs (Faber et al. 2002), given model sources from numerical simulations (Faber et al. 2006; Rantsiou et al. 2008). To date, such analyses have focused on the circular inspiral of BHs with NSs, however recent population synthesis studies suggest the number of BH-NS binaries that form may be as rare as those expected here,  $\sim 1 \text{ yr}^{-1}$  (Belczynski et al. 2007).

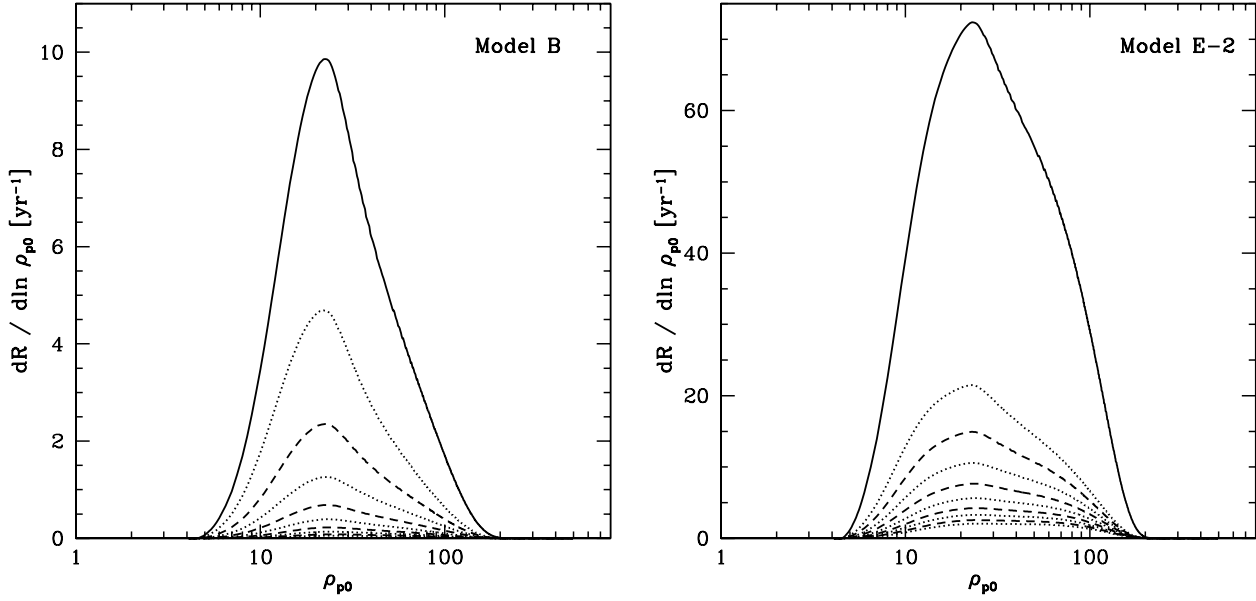


**Figure 12.** The pericenter distribution for AdLIGO detections. Plotted is the differential detection rate ( $dR/d \ln \rho_{p0}$ ) as a function of  $\rho_{p0}$  for Models B (left) and E-2 (right). In both figures, the solid line is differential rate for the all detections, the alternating dotted and dashed lines are for each individual mass bin  $M$  ( $\sum_m dR_{mM}/(2d \ln \rho_{p0})$ ) in order of decreasing mass from top to bottom. Note that function plotted here is different than in Fig. 4

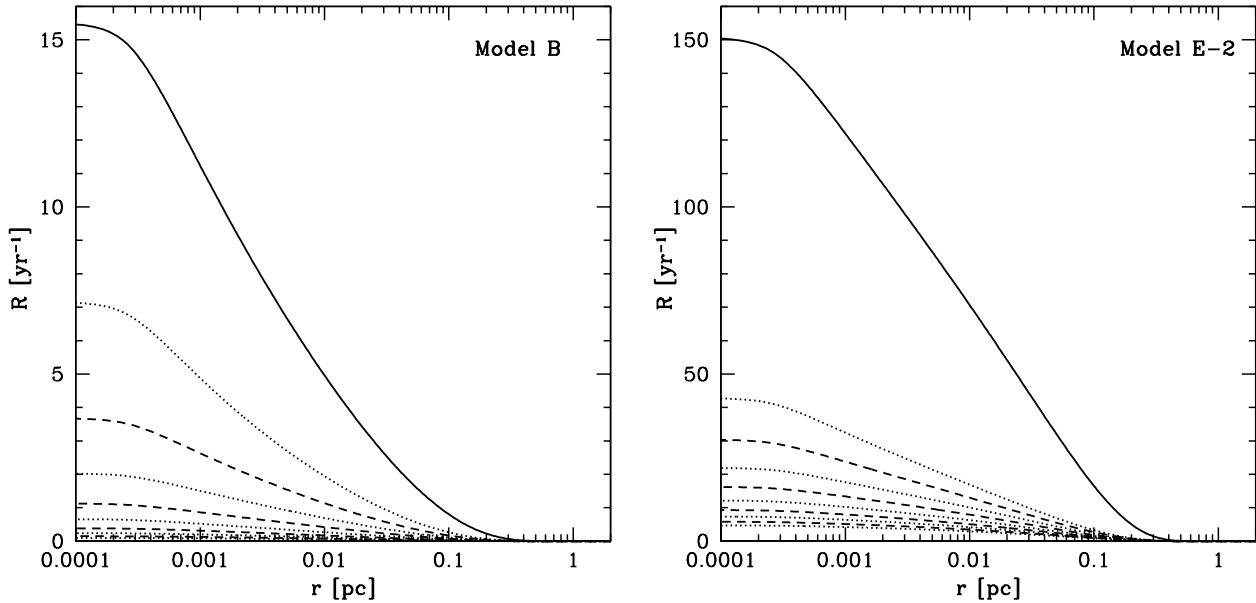


**Figure 13.** The AdLIGO detection rate for Models B and E-2. The solid line is the total integrated AdLIGO detection rate at radii larger than  $r$ , ( $R(> r)$ ), the alternating dotted and dashed lines are the contribution to the detection rate of each individual mass bin ( $\sum_m R_{mM}(> r)/2$ ) in order of decreasing mass from top to bottom.

Given that GW capture binaries are predominately eccentric throughout inspiral, we also expect the newly formed BH-NS binaries to be eccentric. However, with BH-NS binaries, the tidal effects of the BH on the NS can provide an additional source of energy dissipation in the binary, which can enrich the GW signal, and cause it to deviate from the point-mass approximations calculated here. Future numer-

ical simulations with eccentric encounters must be done in order to test the importance of eccentricity on the GW signal for BH-NS binaries.

Another area we neglected is the influence of binarity on the merger rate of BHs in galactic nuclei. However, we can estimate their overall importance by looking at what fraction of binaries are hard enough to survive in galactic nuclei.

Given the distribution of BH binaries in Belczynski et al. (2004), only a small fraction,  $\lesssim 0.1\%$  of the BH-BH binaries are sufficiently hard (with an orbital period  $\lesssim 10$  days) not to be disrupted by repeated encounters with stars or BHs. Interestingly, this fraction is comparable to the fraction of BHs that merge due GW capture. The properties of the merger of such binaries have not been explored yet, however, given the evidence that such encounters produce few eccentric events in massive star clusters, we expect that they will not have many eccentric mergers in galactic nuclei. Unfortunately, the methods we have used here are not suitable for looking at higher order  $N$ -body interactions (such as exchanges, or binary-binary scattering); simulations similar to FAK06 are more adequate for this type of study. The rates we calculated might be enhanced if high-dispersion environments of protogalactic cores without a SMBH also exist, although such systems are old and not long lived (Quinlan & Shapiro 1987, 1989, 1990; Lee 1993).

In order to estimate the detection rate of gravitational wave capture binaries in galactic nuclei we had to make assumptions that introduced uncertainty in our calculations. For the sake of clarity, we wish to summarise these uncertainties and the order of magnitude effect they may have on the actual detection rate for AdLIGO. The largest uncertainty in the rate calculation is the distribution of BHs in galactic nuclei, especially the number fraction of BHs ( $\sim 10^2$ ) and their mass distribution ( $\sim 10$ ) in the centres of galaxies. Observations of our own galactic centre suggest that the star formation may be top-heavy, and place the rate on the higher end of that reported here. One effect we neglect in our calculations is resonant relaxation, which may reduce the rate ( $\sim 10$ ) by depleting the central cusp of BHs. Our final rate, however, is in practice only logarithmically sensitive to the inner edge of the cusp of BHs, and the densest cusps that dominate our rate will be least affected by resonant relaxation. The final rate is also nearly logarithmically dependent on the population of SMBHs in the local universe (by a factor of at most  $\sim 10$ ), but is much more sensitive to the distribution of densities at the radius of influence of the BHs (by a factor of  $\sim 10$ – $10^2$ ). Finally, there is some uncertainty in the detection rate given our calculation of the  $S/N$  of the mergers ( $\sim 10$ ) since we do not consider corrections for zoom-whirl orbits and conservatively ignore the contribution of the merger and ringdown waveforms of the binary to the signal.

There are many aspects to the merger of GW capture binaries that require future work, which will be aided by advanced numerical simulations of the evolution of these binaries. In our calculations we used only the leading order (Newtonian) formula to calculate the evolution of the binaries and the GW waveforms, and do not account for the GW signal during the plunge and merger of the binary, nor do we consider the contribution of zoom-whirl orbits. The recent breakthrough of numerical simulations finally allows the full GW signal to be calculated directly. Eccentric mergers promise to have a richer signal than that for circular binaries. Future studies should incorporate the contribution of the final coalescence to the GW signal, which would increase the signal strength generated during the inspiral for the same capture event, and has a potential to further increase the maximum range of detection.

We also found that a fraction ( $\sim 10 - 20\%$ ) of mergers

will occur very close to, or within the estimated last stable orbit of BH binaries. These capture events may be zoom-whirl orbits, which dramatically increases the GW signal compared to a regular inspiral (Pretorius & Khurana 2007). Such encounters are inherently in the strong GR regime, and again require a full numerical treatment of General Relativity to be studied. A precise assessment of these sources will further increase our estimates of detection rates. Our estimates for the number of GW capture binaries in galactic nuclei (and perhaps in massive star clusters) suggest that such events may be common enough to be directly detected, and may provide the richest gravitational wave sources in the universe for ground based detectors.

## ACKNOWLEDGEMENTS

We thank Krzysztof Belczynski, Sam Finn, Scott Hughes, Pablo Laguna, Ilya Mandel, Szabolcs Márka, and Coleman Miller for useful discussions and András Pál for helping with Figure 9. This work is supported by in part by NASA grant NNX08AL43G, by FQXi, and by Harvard University funds. BK acknowledges support from OTKA Grant 68228 and Polányi Program of the Hungarian National Office for Research and Technology (NKTH).

## REFERENCES

- Abbott et al. 2008, *Phys. Rev. D*, 77, 062002  
 Alexander R. D., Armitage P. J., Cuadra J., Begelman M. C., 2008, *ApJ*, 674, 927  
 Alexander T., Hopman C., 2008, *ApJ*, Submitted, ArXiv:0808.3150  
 Alexander T., Kumar P., 2001, *ApJ*, 549, 948  
 Alexander T., Loeb A., 2001, *ApJ*, 551, 223  
 Alexander T., Sternberg A., 1999, *ApJ*, 520, 137  
 Aller M. C., Richstone D., 2002, *AJ*, 124, 3035  
 Amaro-Seoane P., Gair J. R., Freitag M., Miller M. C., Mandel I., Cutler C. J., Babak S., 2007, *Classical and Quantum Gravity*, 24, 113  
 Arun K. G., Blanchet L., Iyer B. R., Qusailah M. S. S., 2008, *Phys. Rev. D*, 77, 064035  
 Arun K. G., Iyer B. R., Qusailah M. S. S., Sathyaprakash B. S., 2006, *Phys. Rev. D*, 74, 024006  
 Babak S., Fang H., Gair J. R., Glampedakis K., Hughes S. A., 2007, *Phys. Rev. D*, 75, 024005  
 Bahcall J. N., Wolf R. A., 1976, *ApJ*, 209, 214  
 Bahcall J. N., Wolf R. A., 1977, *ApJ*, 216, 883  
 Baker J. G., McWilliams S. T., van Meter J. R., Centrella J., Choi D.-I., Kelly B. J., Koppitz M., 2007, *Phys. Rev. D*, 75, 124024  
 Barack L., Cutler C., 2004, *Phys. Rev. D*, 69, 082005  
 Barth A. J., Greene J. E., Ho L. C., 2005, *ApJ*, 619, L151  
 Belczynski K., Kalogera V., Bulik T., 2002, *ApJ*, 572, 407  
 Belczynski K., Sadowski A., Rasio F. A., 2004, *ApJ*, 611, 1068  
 Belczynski K., Taam R. E., Kalogera V., Rasio F. A., Bulik T., 2007, *ApJ*, 662, 504  
 Berti E., Cardoso J., Cardoso V., Cavaglià M., 2007, *Phys. Rev. D*, 76, 104044

- Binney J., Tremaine S., 1987, *Galactic dynamics*. Princeton, NJ, Princeton University Press, 1987, 747 p.
- Boyle M., Buonanno A., Kidder L. E., Mroué A. H., Pan Y., Pfeiffer H. P., Scheel M. A., 2008, ArXiv:0804.4184
- Brown D. A., Brink J., Fang H., Gair J. R., Li C., Lovelace G., Mandel I., Thorne K. S., 2007, *Physical Review Letters*, 99, 201102
- Brown W. R., Geller M. J., Kenyon S. J., Kurtz M. J., 2005, *ApJ*, 622, L33
- Brown W. R., Geller M. J., Kenyon S. J., Kurtz M. J., 2006, *ApJ*, 640, L35
- Chanamé J., Gould A., Miralda-Escudé J., 2001, *ApJ*, 563, 793
- Chanamé, J., & Gould, A. 2002, *ApJ*, 571, 320
- Collins N. A., Hughes S. A., 2004, *Phys. Rev. D*, 69, 124022
- Côté P., Blakeslee J. P., Ferrarese L., Jordán A., Mei S., Merritt D., Milosavljević M., Peng E. W., Tonry J. L., West M. J., 2004, *ApJS*, 153, 223
- Damour T., Gopakumar A., Iyer B. R., 2004, *Phys. Rev. D*, 70, 064028
- Deegan P., Nayakshin S., 2007, *MNRAS*, 377, 897
- Eisenhauer F., Genzel R., Alexander T., Abuter R., Paumard T., Ott T., et al. 2005, *ApJ*, 628, 246
- Faber J. A., Baumgarte T. W., Shapiro S. L., Taniguchi K., Rasio F. A., 2006, *Phys. Rev. D*, 73, 024012
- Faber J. A., Grandclément P., Rasio F. A., Taniguchi K., 2002, *Physical Review Letters*, 89, 231102
- Flanagan É. É., Hughes S. A., 1998, *Phys. Rev. D*, 57, 4535
- Freitag M., Amaro-Seoane P., Kalogera V., 2006, *ApJ*, 649, 91
- Gair J. R., Barack L., Creighton T., Cutler C., Larson S. L., Phinney E. S., Vallisneri M., 2004, *Classical and Quantum Gravity*, 21, 1595
- Gair J. R., Kennefick D. J., Larson S. L., 2005, *Phys. Rev. D*, 72, 084009
- Gair J. R., Kennefick D. J., Larson S. L., 2006, *Phys. Rev. D*, 74, 109901
- Genzel R., Schödel R., Ott T., Eisenhauer F., Hofmann R., Lehnert M., Eckart A., Alexander T., Sternberg A., Lenzen R., Clénet Y., Lacombe F., Rouan D., Renzini A., Tacconi-Garman L. E., 2003, *ApJ*, 594, 812
- Ghez A. M., Salim S., Hornstein S. D., Tanner A., Lu J. R., Morris M., Becklin E. E., Duchêne G., 2005, *ApJ*, 620, 744
- Greene J. E., Ho L. C., 2006, *ApJ*, 641, L21
- Greene J. E., Ho L. C., Barth A. J., 2008, *ApJ*, 688, 159
- Gültekin K., Miller M. C., Hamilton D. P., 2004, *ApJ*, 616, 221
- Gültekin K., Miller M. C., Hamilton D. P., 2006, *ApJ*, 640, 156
- Hinder I., Herrmann F., Laguna P., Shoemaker D., 2008, ArXiv:0806.1037
- Hinder I., Vaishnav B., Herrmann F., Shoemaker D. M., Laguna P., 2008, *Phys. Rev. D*, 77, 081502
- Hopman C., Alexander T., 2006a, *ApJ*, 645, 1152
- Hopman C., Alexander T., 2006b, *ApJ*, 645, L133
- Hopman C., Freitag M., Larson S. L., 2007, *MNRAS*, 378, 129
- Kalogera V., Kim C., Lorimer D. R., Burgay M., D’Amico N., Possenti A., Manchester R. N., Lyne A. G., Joshi B. C., McLaughlin M. A., Kramer M., Sarkissian J. M., Camilo F., 2004b, *ApJ*, 614, L137
- Kalogera V., Kim C., Lorimer D. R., Burgay M., D’Amico N., Possenti A., Manchester R. N., Lyne A. G., Joshi B. C., McLaughlin M. A., Kramer M., Sarkissian J. M., Camilo F., 2004a, *ApJ*, 601, L179
- Kocsis B., Gáspár M. E., Márka S., 2006, *ApJ*, 648, 411
- Kroupa P., Weidner C., 2003, *ApJ*, 598, 1076
- Kulkarni S. R., Hut P., McMillan S., 1993, *Nat*, 364, 421
- Lee M. H., 1993, *ApJ*, 418, 147
- Levin J., 2006, *Phys. Rev. D*, 74, 124027
- Levin, J., & Perez-Giz, G. 2008, *Phys. Rev. D*, 77, 103005
- Majar J., Vasuth M., 2008, *Phys. Rev. D*, 77, 104005
- Mandel I., Brown D. A., Gair J. R., Miller M. C., 2008, *ApJ*, 681, 1431
- Maness H., Martins F., Trippe S., Genzel R., Graham J. R., Sheehy C., Salaris M., Gillessen S., Alexander T., Paumard T., Ott T., Abuter R., Eisenhauer F., 2007, *ApJ*, 669, 1024
- Martel K., 2004, *Phys. Rev. D*, 69, 044025
- Martel K., Poisson E., 1999, *Phys. Rev. D*, 60, 124008
- Merritt D., Mikkola S., Szell A., 2007, *ApJ*, 671, 53
- Merritt D., Piatek S., Portegies Zwart S., Hemsendorf M., 2004, *ApJ*, 608, L25
- Miller M. C., Lauburg V. M., 2009, *ApJ*, 692, 917
- Miralda-Escudé J., Gould A., 2000, *ApJ*, 545, 847
- Morris M., 1993, *ApJ*, 408, 496
- Muno M. P., Bauer F. E., Bandyopadhyay R. M., Wang Q. D., 2006, *ApJS*, 165, 173
- Muno M. P., Pfahl E., Baganoff F. K., Brandt W. N., Ghez A., Lu J., Morris M. R., 2005, *ApJ*, 622, L113
- Nayakshin S., Dehnen W., Cuadra J., Genzel R., 2006, *MNRAS*, 366, 1410
- Nayakshin S., Sunyaev R., 2005, *MNRAS*, 364, L23
- Nayakshin S., Sunyaev R., 2007, *MNRAS*, 377, 1647
- O’Leary R. M., Loeb A., 2008, *MNRAS*, 383, 86
- O’Leary R. M., O’Shaughnessy R., Rasio F. A., 2007, *Phys. Rev. D*, 76, 061504
- O’Leary R. M., Rasio F. A., Fregeau J. M., Ivanova N., O’Shaughnessy R., 2006, *ApJ*, 637, 937
- Orosz J. A., McClintock J. E., Narayan R., Bailyn C. D., Hartman J. D., Macri L., Liu J., Pietsch W., Remillard R. A., Shporer A., Mazeh T., 2007, *Nat*, 449, 872
- Paumard T., Genzel R., Martins F., Nayakshin S., Beloborodov A. M., Levin Y., Trippe S., Eisenhauer F., Ott T., Gillessen S., Abuter R., Cuadra J., Alexander T., Sternberg A., 2006, *ApJ*, 643, 1011
- Peters P. C., 1964, *Physical Review*, 136, 1224
- Peters P. C., Mathews J., 1963, *Physical Review*, 131, 435
- Portegies Zwart S. F., Baumgardt H., McMillan S. L. W., Makino J., Hut P., Ebisuzaki T., 2006, *ApJ*, 641, 319
- Portegies Zwart S. F., McMillan S. L. W., 2000, *ApJ*, 528, L17
- Prestwich A. H., Kilgard R., Crowther P. A., Carpano S., Pollock A. M. T., Zezas A., Saar S. H., Roberts T. P., Ward M. J., 2007, *ApJ*, 669, L21
- Pretorius F., Khurana D., 2007, *Classical and Quantum Gravity*, 24, 83
- Quinlan G. D., Shapiro S. L., 1987, *ApJ*, 321, 199
- Quinlan G. D., Shapiro S. L., 1989, *ApJ*, 343, 725
- Quinlan G. D., Shapiro S. L., 1990, *ApJ*, 356, 483
- Rantsiou E., Kobayashi S., Laguna P., Rasio F. A., 2008, *ApJ*, 680, 1326
- Rauch K. P., Ingalls B., 1998, *MNRAS*, 299, 1231
- Rauch K. P., Tremaine S., 1996, *New Astronomy*, 1, 149

- Remillard R. A., McClintock J. E., 2006, *ARA&A*, 44, 49
- Rubbo L. J., Holley-Bockelmann K., Finn L. S., 2006, *ApJ*, 649, L25
- Sadowski A., Belczynski K., Bulik T., Ivanova N., Rasio F. A., O’Shaughnessy R., 2008, *ApJ*, 676, 1162
- Schödel R., Eckart A., Alexander T., Merritt D., Genzel R., Sternberg A., Meyer L., Kul F., Moulata J., Ott T., Straubmeier C., 2007, *A&A*, 469, 125
- Sesana A., Haardt F., Madau P., 2007, *MNRAS*, 379, L45
- Shapiro S. L., Lightman A. P., 1976, *Nat*, 262, 743
- Sigurdsson S., Hernquist L., 1993, *Nat*, 364, 423
- Silverman J. M., Filippenko A. V., 2008, *ApJ*, 678, L17
- Sperhake U., Berti E., Cardoso V., Gonzalez J. A., Bruegmann B., Ansorg M., 2008, *PhRvD*, 78, 064069
- Spitzer L. J., 1969, *ApJ*, 158, L139+
- Tanaka T., Tagoshi H., Sasaki M., 1996, *Progress of Theoretical Physics*, 96, 1087
- Tessmer M., Gopakumar A., 2008, *PhRvD*, 78, 084029
- Tremaine S., Gebhardt K., Bender R., Bower G., Dressler A., Faber S. M., Filippenko A. V., Green R., Grillmair C., Ho L. C., Kormendy J., Lauer T. R., Magorrian J., Pinkney J., Richstone D., 2002, *ApJ*, 574, 740
- Turner M., 1977, *ApJ*, 216, 610
- Vasuth M., Majar J., 2007, *Int. J. Mod. Phys.*, A22, 2405
- Washik M. C., Healy J., Herrmann F., Hinder I., Shoemaker D. M., Laguna P., Matzner R. A., 2008, *PhRvL*, 101, 061102
- Watters W. A., Joshi K. J., Rasio F. A., 2000, *ApJ*, 539, 331
- Weinberg N. N., Milosavljević M., Ghez A. M., 2005, *ApJ*, 622, 878
- Wen L., 2003, *ApJ*, 598, 419
- White N. E., van Paradijs J., 1996, *ApJ*, 473, L25+
- Willems B., Henninger M., Levin T., Ivanova N., Kalogera V., McGhee K., Timmes F. X., Fryer C. L., 2005, *ApJ*, 625, 324
- Wu X., Xie Y., 2007, *Phys. Rev. D*, 76, 124004
- Yunes N., Sopuerta C. F., Rubbo L. J., Holley-Bockelmann K., 2008, *ApJ*, 675, 604